

JGR Solid Earth

RESEARCH ARTICLE

10.1029/2023JB026843

Key Points:

- We present a method that embeds repeaters-derived slip rates into the neighboring fault patch for geodetic data inversion
- We achieve a higher resolution of inter-seismic slip rate distribution below a depth of 10 km, on a seaward-dipping thrust fault
- The inferred low coupling ratio establishes an extensive creeping area, coinciding with the location of active repeaters and swarm events

Supporting Information:

Supporting Information may be found in the online version of this article.

Correspondence to:

K. H. Chen,
katepili@gmail.com

Citation:

Peng, W., Radiguet, M., Pathier, E., & Chen, K. H. (2023). Fault coupling on a creeping thrust fault: Joint inversion using geodetic data and repeating earthquakes. *Journal of Geophysical Research: Solid Earth*, 128, e2023JB026843. <https://doi.org/10.1029/2023JB026843>

Received 2 APR 2023

Accepted 2 SEP 2023

Author Contributions:

Conceptualization: Mathilde Radiguet, Erwan Pathier, Kate Huihsuan Chen
Data curation: Erwan Pathier
Investigation: Wei Peng
Methodology: Mathilde Radiguet, Erwan Pathier
Supervision: Mathilde Radiguet, Erwan Pathier, Kate Huihsuan Chen
Validation: Wei Peng, Mathilde Radiguet, Erwan Pathier
Writing – original draft: Wei Peng
Writing – review & editing: Kate Huihsuan Chen

Fault Coupling on a Creeping Thrust Fault: Joint Inversion Using Geodetic Data and Repeating Earthquakes

Wei Peng^{1,2} , Mathilde Radiguet² , Erwan Pathier² , and Kate Huihsuan Chen¹ 

¹Department of Earth Sciences, National Taiwan Normal University, Taipei, Taiwan, ²Univ. Grenoble Alpes, Univ. Savoie Mont Blanc, CNRS, IRD, Univ. Gustave Eiffel, ISTerre, Grenoble, France

Abstract Due to the lack of recognized creep on dip-slip faults, the nature of fault creep and its role in the generation of large earthquakes is largely unexplored. The Chihshang fault in Taiwan serves as one of the best examples of a thrust creeping fault in the world, exhibiting a fast creep rate of 2–3 cm/year and the capability of producing magnitude six earthquakes. Land-based geodetic measurements are less sensitive to fault slip with depth, especially for the deeper portion of the seaward dipping fault. Taking advantage of slip rates inferred from repeating earthquake sequences (RESs) at greater depths (up to 30 km), we present a method that embeds RES-derived slip rates into the neighboring fault patch for geodetic data inversion. Using the geodetic and seismological data from 2007 to 2011, we achieve a higher resolution of inter-seismic slip rate distribution below a depth of 10 km. The inferred low coupling ratio establishes an extensive creeping area that coincides with a location of abundant RES and earthquake swarms. The inferred high coupling ratio, on the other hand, delineates a locked area corresponding to the two co-seismic slip zones of the 2003 Mw 6.8 Chengkung and 2022 Mw 6.7 Yuli earthquakes. The transition zone marking the gradual change from fully locked to shallow creeping areas appears to coincide with the post-seismic slip area of the 2003 Chengkung event. Using the fault coupling model, the moment rate deficit measured in the two locked areas is capable of generating a M_w 6.8 event every 78 years to the south and a M_w 6.7 event every 28 years to the north. This moment rate deficit is decreased by 10% when the closely located Central Range fault is considered in a two-fault model, leading to the slightly longer recurrence interval on the Chihshang fault. The two-fault model potentially contributes to a better understanding of the regional inter-seismic deformation, which is recommended to be adopted in the future studies of seismic hazard assessment.

Plain Language Summary Large earthquakes can occur on the creeping faults that slowly slip at the surface but accumulate energy at greater depth. How much different portions of the fault slip annually is the key question for seismic hazard assessment. However, for a seaward-dipping thrust fault like the Chihshang fault in Taiwan, finding the answer is difficult because the loss of resolution at the greater depth (>10 km) due to a lack of offshore data. Taking advantage of the slip rates inferred from repeating earthquakes that mainly occurred at 10–30 km depth, we present a method that embeds repeating events data into the geodetic inversion for higher resolution of inter-seismic slip model. We found that the areas slipped faster during the inter-seismic period (higher inter-seismic slip rate) coincides with the location of abundant repeating earthquakes and swarm events; The areas with lower inter-seismic slip rate on the other hand, correspond to the zones that slipped during the 2003 M_w 6.8 Chengkung and 2022 M_w 6.7 Yuli earthquakes. By calculating how much and where the seismic energy was released through inter-seismic slip rate, we are able to identify two separate zones on the Chihshang fault that is capable of generating a $\sim M_w$ 6 event every 28 to the north and 78 years to the south of the fault, respectively.

1. Introduction

Understanding the interplay between seismic and aseismic fault slip is crucial for evaluating the stress accumulation on a fault and for assessing the potential seismic hazard. The development of modern geodetic monitoring enables the exploration of aseismic slip behavior in space and time. Fault creep, as part of the steady sliding of a fault surface, has been observed in tectonically active continental regions worldwide, mostly on strike-slip faults and on many subduction thrusts (Bürgmann, 2018). Creeping thrust and normal faults, however, are rare in tectonically active continental regions (Harris, 2017). Owing partly to few recognized creeps on dip-slip faults, the nature of fault creep and its role in the generation of large earthquakes remains largely unknown. The Chihshang fault in Taiwan serves as one of the best examples of a fault with a primarily thrust component

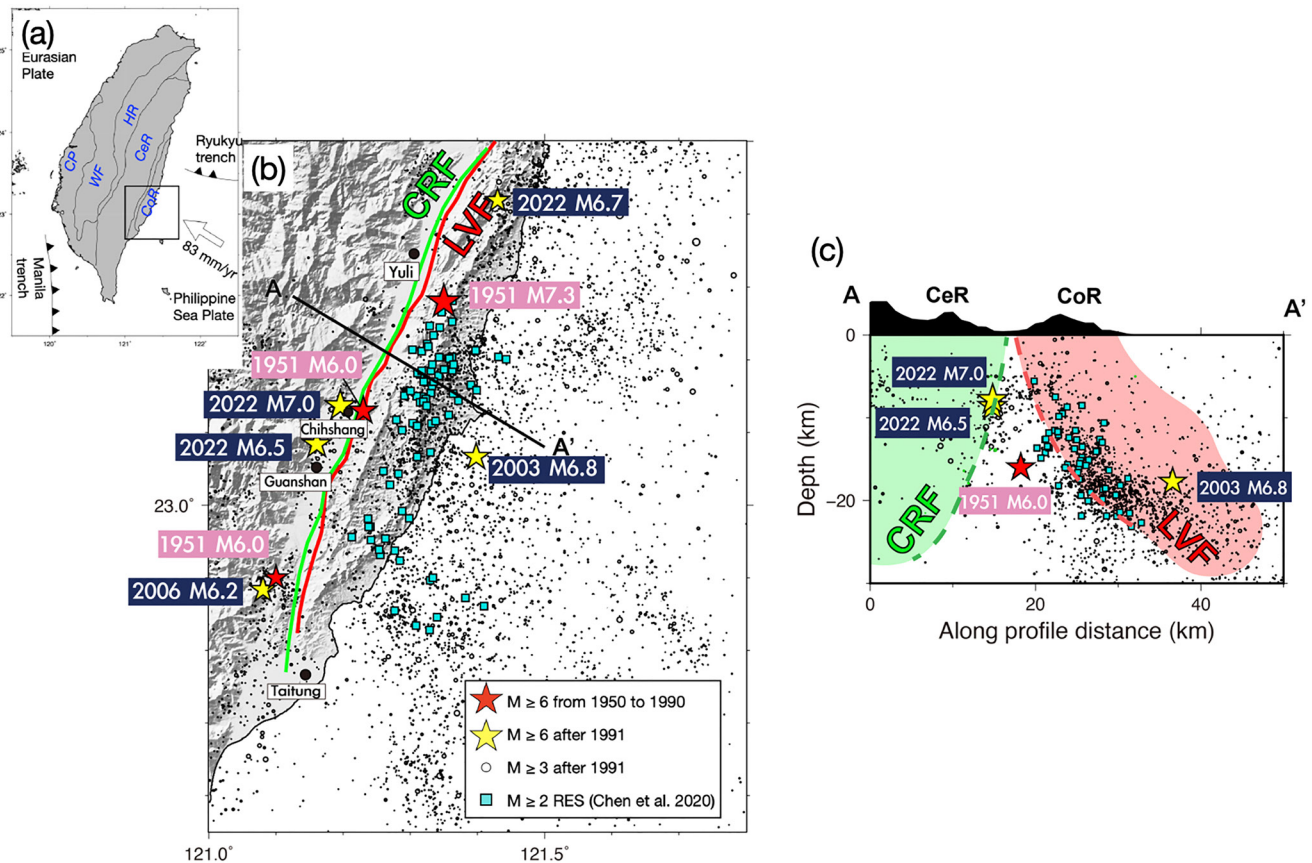


Figure 1. (a) Simplified tectonic setting of Taiwan. Tectonic units from west to east are the Coastal Plain (CP), the Western Foothills (WF), the Hsuehshan Range (HR), the Central Range (CeR) and the Coastal Range (CoR). The black rectangle marks the area shown in (b). (b) Map of the study area. Green and red solid lines indicate the Central Range fault (CRF) and the Chihshang segment of the Longitudinal Valley fault (LVF) respectively. Red and yellow stars represent the $M_L \geq 6$ events occurred during 1950–1990 and 1991–2022, respectively. Open black circles and filled cyan squares represent the $M_L \geq 3$ background seismicity and the $M_L \geq 2$ repeating earthquake sequences (RES), respectively. Fault segmentation of the LVF and CRF is from K. H. Chen et al. (2007) and W.-S. Chen et al. (2020), respectively. (c) Cross sections of AA' donated in figure (a), respectively. The symbols as the same in (a). The earthquake information corresponding to each star is shown in Table 1.

that rapidly creeps at the surface. It is known to have produced three magnitude six earthquakes during the past hundred years.

As an active plate boundary between the Philippine Sea Plate (PSP) and Eurasian Plate, the Longitudinal Valley in eastern Taiwan is an example of extreme strain concentration in an oblique collision zone (e.g., Angelier et al., 1997) (Figure 1a). This boundary is composed of two parallel and close-spacing structures (Figure 1b) with opposite dipping directions: the east-dipping Longitudinal Valley fault (LVF) to the east and the west-dipping Central Range fault (CRF) to the west (Shyu et al., 2005, 2007), as denoted by red and green lines in Figures 1b and 1c, respectively. These two opposite-dipping, reverse-dominated dip-slip faults intersect near the surface as a result of the ongoing suturing process and rapid exhumation of the Central Range (CeR). The seismicity in the study area is mainly distributed to the south of 23.5°N and north of 22.5°N (Figure 1b), which form the east-dipping structure underneath Coastal Range (CoR) and the steeply west-dipping structure beneath the valley, as revealed by the two separate earthquake clusters in Figure 1c with the denotation of red and green dashed lines as LVF and CRF, respectively.

Historically, LVF had ruptured intensively during the 1951 earthquake sequence (called 1951 H-T sequence) that is composed of 12 $M_L \geq 6$ events at several segments along the 150-km-long fault (e.g., Cheng et al., 1996); Three earthquakes occurred in this study area (M7.3 event in Yuli, two M6.0 events in Chihshang and Taitung), as indicated by the red stars in Figure 1b. In the following 55 years, the study area had been quiet seismically. Since 2003, both the LVF and CRF have hosted several $M_w \geq 6$ events (yellow stars in Figure 1b), while three events showing

Table 1
Historical Earthquakes in the Study Area

Time (DD/MM/YYYY)	Longitude (°)	Latitude (°)	Depth (km)	ML reported by CWB	M _w reported by CWB	(Strike,dip,rake) (°)	Name	Responsible fault
24 November 1951	121.2250	23.1250	16.00	6.0	x	(32,70,70)	1951 H-T sequence	LVF (Shyu et al., 2007)
24 November 1951	121.3500	23.2750	36.00	7.3	x	(25,70,40)	1951 H-T sequence	CRF (Shyu et al., 2007)
26 November 1951	121.1000	22.9000	0.00	6.0	x	(8,55,90)	1951 H-T sequence	LVF (K. H. Chen, Toda, & Rau, 2008)
10 December 2003	121.3981	23.0666	17.73	6.4	6.8	(5,61,91) (AutoBATs)	Chengkung eq	LVF (Ching et al., 2007)
1 April 2006	121.0806	22.8835	7.20	6.2	6.2	(177,72,10) (AutoBATs)	Taitung eq	CRF (Mozziconacci et al., 2013)
22 March 2022	121.6118	23.3985	25.73	6.7	6.7	(13,56,71) (AutoBATs)	Yuli eq	
17 September 2022	121.1608	23.0840	8.61	6.6	6.5	(202,62,15) (AutoBATs)	Guanshan-Chihshang eq	CRF (S.-J. Lee et al., 2023)
18 September 2022	121.1958	23.1370	7.81	6.8	7.0	(211,56,40) (AutoBATs)	Guanshan-Chihshang eq	CRF (S.-J. Lee et al., 2023)

Note. CWB, Central Weather Bureau.

the LVF-CRF interaction due to the closeness of aftershock activities in space and time: 2003 M_w 6.8 Chengkung earthquake, 2006 M_w 6.2 Taitung earthquake and the most recent 2022 M_w 7.0 and M_w 6.5 Guanshang-Chihshang earthquake sequence (K. H. Chen, Toda, & Rau, 2008; Kuochen et al., 2007; S.-J. Lee et al., 2023; Mozziconacci et al., 2013; Wu et al., 2006). The information of historical earthquakes can be seen in Table 1. Inter-seismically, the dominant structures of the study area have been accommodating ~ 4 cm/year shortening (e.g., Liu & Yu, 1990), which is mostly taken up across the east-dipping creeping segment of the LVF (the Chihshang fault). The western dipping CRF, however, is likely locked during the inter-seismic period with up to 12.8 mm/year slip rate (Shyu et al., 2006). How the closeness of the two fault systems complicates the inter-seismic behavior of the Chihshang fault remains unclear. With the attempt to establish the present-day kinematic behavior of the creeping fault, we hope to better explore the inter-seismic slip rate model by (a) a joint inversion using geodetic and repeating earthquake data and (b) a consideration of the adjacent CRF in the modeling configuration.

2. The Creeping Chihshang Fault

Using Global Positioning System (GPS), trilateration, creepmeters, and leveling data, a velocity discontinuity of ~ 3 cm/year across the Chihshang fault has been attributed to shallow aseismic creep. The shortening rate across the fault measured by trilateration surveys is 1.4–2.7 cm/year, which makes this fault account up to 24% of the total shortening across the Taiwan collision in the N54°W direction of relative motion between the PSP and the Taiwan Strait (Angelier et al., 1997). Hsu et al. (2003) inferred a creep rate of 2.8–3.3 cm/year at shallow depths (< 8 km) and 4.8–6.2 cm/year at greater depths along a sub-horizontal decollement. Adding constraints from satellite synthetic aperture radar Interferometry (InSAR) allows for higher spatial resolution of inter-seismic slip rates near the surface. Using ALOS-1 satellite data from 2007 to 2011 with the Permanent Scatterer InSAR technique (PS-InSAR), Champenois et al. (2012) obtained the density of geodetic measurements of up to 50 points/km² in the study area. The velocity offsets across the Chihshang fault were found to be 1–3 cm/year along the radar line-of-sight (LOS). Using 1992–2010 GPS and ALOS-1 PS-InSAR data, Thomas et al. (2014) obtained a coupling model to establish that the locked zone in the Chihshang fault coincides with the co-seismic slip area of the 2003 M_w 6.8 Chengkung earthquake. They concluded that the resolution of deeper creep (> 10 km depth) is quite limited owing to the seaward-dipping fault geometry. Despite that the numerous observational studies aimed at a better understanding of the inter-seismic slip behavior, a definitive resolution of how and where the fault creeps remains to be explored.

The Chihshang fault has been recognized as a listric thrust fault that ruptured during the 1951 M_L 6.0 Chihshang event (red star denoted by “1951 M6.0” near Chihshang town in Figure 1b), 2003 M_w 6.8 Chengkung event (yellow star offshore), and 2022 M_w 6.7 Yuli event (yellow star in the north of the study area). The recurrence intervals and seismic moments of a repeating earthquake sequence (RES) have been found to provide important information of fault creep at the precise location of events (Bürgmann et al., 2000; Nadeau & Johnson, 1998; Nadeau & McEvilly, 1999). On the Chihshang fault, RESs are found to mostly occur below 10 km depth (cyan squares in Figures 1b and 1c), which provides an independent set of deep slip rate measurements in the study area (K. H. Chen, Nadeau, & Rau, 2008; K. H. Chen et al., 2009; Y. Chen et al., 2020). During the study period of 1991–2004, RESs were found to reveal the deep creep rate ranging from 2.0 to 5.1 cm/year (K. H. Chen, Nadeau, & Rau, 2008). The extended RESs catalog from 2000 to 2011 (Y. Chen et al., 2020) revealed the acceleration of deep creep rate up to 12.3 cm/year at the time of the M_w 6.8 Chengkung earthquake, then dropped to 4.1 cm/year until the end of 2011. Unlike the regional slip rate derived from RESs (Y. Chen et al., 2020) and the kinematic model inverted solely using geodetic data (Thomas et al., 2014), here we aim to combine both geodetic and RESs measurements into an integrated inter-seismic slip model, to obtain a better resolved slip behavior on this thrust creeping fault. The combination of these independent data sets raises several questions: What

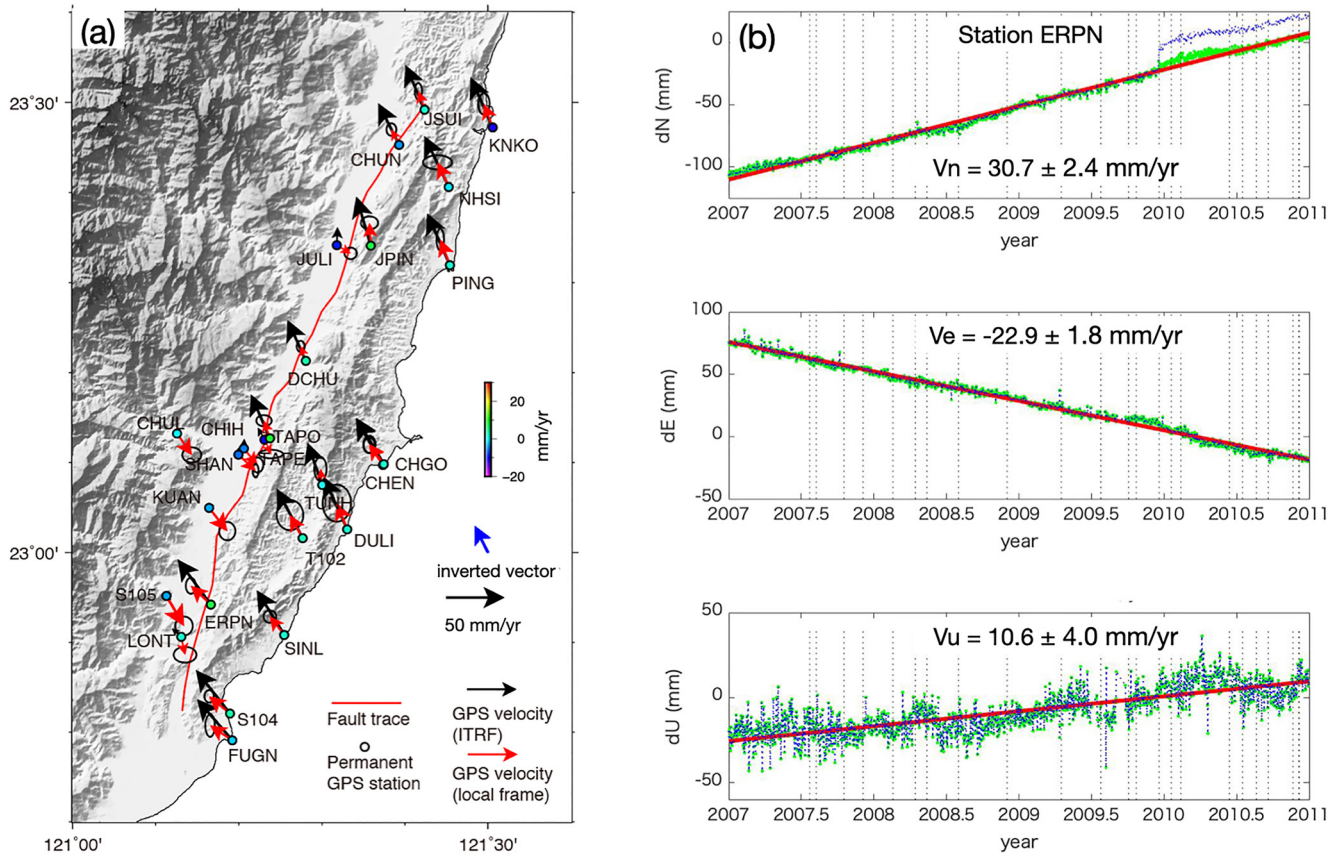


Figure 2. (a) Location of Global Positioning System (GPS) stations (colored circles) used in this study. The red line represents the fault trace of the Chihshang segment of the Longitudinal Valley fault. Black arrows represent horizontal velocity vector in International Terrestrial Reference System (ITRF) reference frame; red arrows in a local reference frame. The blue arrow is the constant vector estimated from our inversion scheme and applied at each station for the transfer from ITRF to the local reference frame. The filled circles indicate the vertical slip rate, which is color coded by the amplitude. (b) Time series of the north–south, east–west, and vertical components of displacement recorded at GPS station ERPN. Vertical dashed lines represent $M_L \geq 5$ events in the study area. Blue dots represent the original time series and green dots represent the corrected time series in which co-seismic effects of the $M_L \geq 5$ events are removed. The numbers V_n , V_e and V_u indicate the GPS inter-seismic velocities estimated using linear regression denoted by red line.

are the data quality assessments, sensitivity tests, and data weightings that should be considered in the inversion procedure? How much does the joint inversion enhance our understanding of aseismic and seismic fault slips? How can the consideration of both the LVF and CRF contribute to seismic hazard estimates? These questions are highlighted in this study.

In the following Section 3, we introduce the different data sets used in the inversion (GPS, InSAR, and RESs) and assess their consistency. In Section 4, we explain a modeling scheme implementing RESs observations in the joint inversion. In Section 5, we present the inter-seismic slip model that illustrates the along-strike variation of slip rate with depth. The coupling ratio is also calculated to compare it with the regional seismicity and aseismic slip driving seismic phenomena. In Section 6, we also demonstrate the kinematic model that considers the contribution of the adjacent CRF and finally, we discuss the advantages and limitations of the inversion results and the implication of the inferred coupling model for regional seismic hazard assessment.

3. Data

3.1. GPS Data

The inter-seismic displacement rates were determined using data from 26 continuous GPS stations in the Chihshang area. The study period, 12 January 2007 to 7 September 2010, was chosen to coincide with the period for which InSAR data were available (detailed in Section 3.2). The raw data (time series) were originally processed in the GPS laboratory of the Institute of Earth Science, Academia Sinica (blue dots in Figure 2b).

Under the International Terrestrial Reference System (ITRF2008), the station coordinates were estimated using the GipsyX (the new version of the GIPSY/OASIS software, <https://gipsy-oasis.jpl.nasa.gov/>), developed by the Jet Propulsion Laboratory (Bertiger et al., 2020). The velocity rate was then determined by the linear regression of the 500 data sets randomly chosen from the time range of 2–4 years (red lines in Figures 2b–2d). As the result, the ITRF velocity field is shown by black arrows in Figure 2a, while the uncertainty defined by standard deviation from the 500 bootstrap samples is indicated by ellipses. To confirm that the GPS data during the 4-year time span can represent the velocity estimate from the long-term motion, we also perform a sensitivity test in Figure S1 in Supporting Information S1. It shows that the velocity rate of GPS from 1994 to 2019 is highly correlated with the one from the study period of 2007–2011.

According to the conventional elastic dislocation model by Savage (1983), the observed surface deformation during inter-seismic period is a combined effect of slip on fault, block rotation (scalar motion), and a constant fault creep below the bottom depth of a fault, as represented by

$$d_{\text{GPS}} = \begin{bmatrix} G_{\text{GPS}} & G_{\text{GPS}} & G_{\text{vector}} \end{bmatrix} \begin{bmatrix} m_{\text{slip}} \\ m_{\text{creep}} \\ m_{\text{vector}} \end{bmatrix}, \quad (1)$$

where d_{GPS} is the observed deformation as indicated by the black arrows in Figure 2a. G_{GPS} is the green's function (Okada, 1992) for estimating the slip at fault (m_{slip}) and the slip at greater depth (m_{creep}). G_{vector} is a designed identity matrix approximated by a 2-Dimensional constant secular motion (eastward and northward motions of m_{vector}) of a block model. By assuming 40 mm/year creep rate at the deeper part of the Chihshang fault (Thomas et al., 2014; Tsai et al., 2015), both m_{slip} and m_{vector} can be inverted based on Equation 1. Note that m_{vector} is resolved at each station, whereas m_{slip} is resolved at each fault patch. We next obtained the local velocity at the surface (red arrows in Figure 2a) by subtracting the secular motion of the block (blue arrows in Figure 2a) from the raw data (black arrows in Figure 2a). The resulting local velocity transfers the ITRF reference frame to the local fault frame, which represents the contribution from faulting in this small area (several tens km).

3.2. InSAR Data

To increase the spatial resolution of the displacement field, we also used the InSAR data provided by Thomas et al. (2014) that estimated the relative fault motion following Champenois et al. (2012). In their work, SAR data were taken from L-band ascending ALOS-1 PALSAR images (wavelength 23.6 cm) processed using a Persistent Scatterer (PS) approach during the study period, 2007–2010 (Ferretti et al., 2001; Hooper et al., 2007). The total number of PS points in the study area was 77,133 with the relative velocity in the radar LOS direction ranging from −51 to 65 mm/year (Figure 3a) with uncertainty in the range 0.26–8.99 mm/year. To remove local outliers in the PS data and reduce the computational cost in the inversion, we downsampled the PS points through spatial smoothing. We smoothed the PS measurements into a regular grid with sizes of $0.01^\circ \times 0.01^\circ$, which results in 1,077 PS grid cells (the number of PS points within a grid cell ranged from 1 to 2,553). As such, the local spatial variability in the original data (Figure 3a) can be largely reduced (Figure 3b), while the original trend along the strike of the fault remains. As shown by the cross-section A–A' (Figure 3c), the short-distance variability in the original data is also diminished by the spatial smoothing. Note that >40% of the 1,077 grids contain fewer than 10 PS points, therefore for each grid cell, we estimated the mean velocity and mean uncertainty using all the PS data and multiplied the mean uncertainty by the standard error. This error is called the weighting factor as indicated by the size of the circles in Figure 3b, which provides the information of velocity reliability in the following inversion.

To check the consistency between the GPS measurements and the InSAR results (raw point-scatterer measurements), we first estimated the mean PS velocity and mean incidence angle of original PS points located within a 500 m radius of each GPS station. The relative GPS velocity (red arrows in Figure 2a) was then projected onto the radar LOS direction based on the mean incidence angle in each station. Figure 4 shows the comparison of InSAR and GPS data, where the uncertainties are represented by horizontal and vertical and lines, respectively. Here the original data points are replicated 100 times by a random selection within the range of data uncertainty. The 100 regression lines are shown by gray lines in Figure 4, which reveals the ratio of GPS/InSAR ranging from

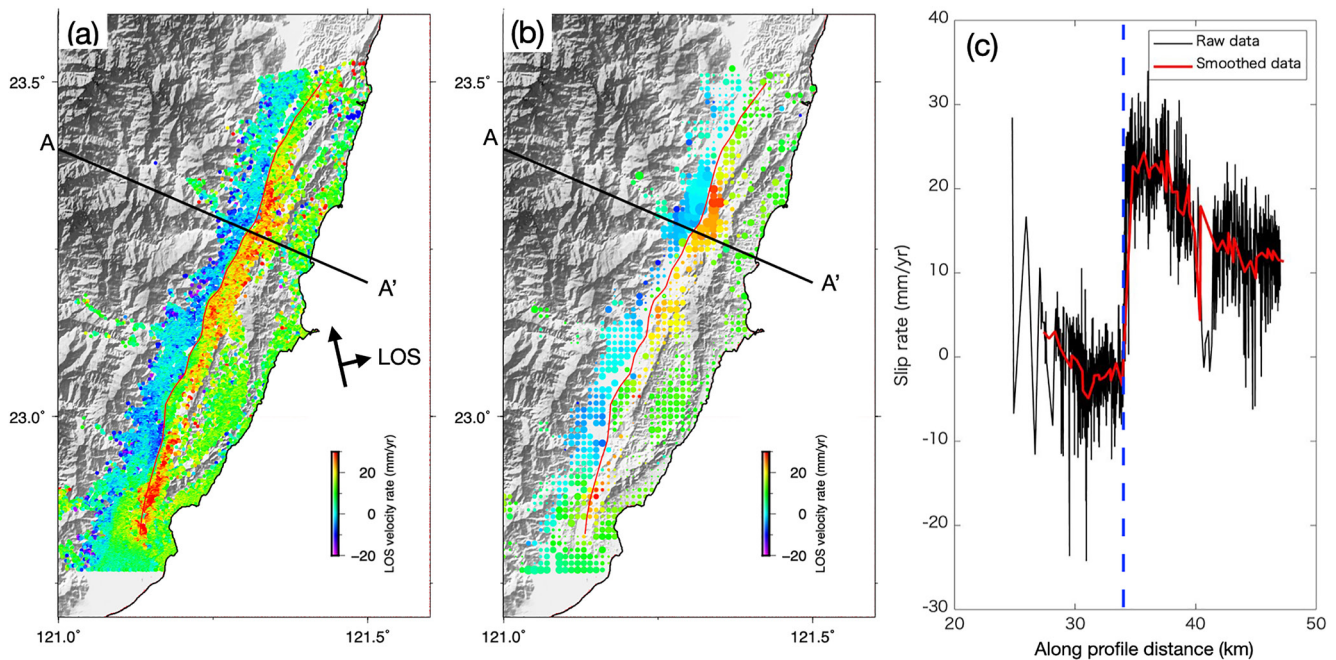


Figure 3. (a) The distribution of Persistent Scatterer (PS) synthetic aperture radar Interferometry (InSAR) displacement rates along the radar line-of-sight (LOS) from all 77,133 PS points during the study period 2007 to 2010. Black arrows show the ascending track direction and the average incidence angle of LOS (37° relative to the vertical). (b) The distribution of 1,077 "smoothed" LOS displacement rates resampled on a $0.01^\circ \times 0.01^\circ$ grid. Each circle represents a grid cell with the color indicating mean LOS displacement rates, while its size is proportional to the weighting factor used in inversion. This factor depends on the number of points within a grid cell and their uncertainties. The red line indicates the Chihshang fault. (c) A comparison between the raw data from (a) and smoothed data from (b) along the same profile A–A' with the projected width of 2 km. The vertical dashed line indicates the location of the fault trace.

0.55 to 1.0 with the mean value of 0.75 ± 0.18 . This suggests that InSAR data are generally in good agreement with GPS measurements.

3.3. Repeating Earthquake Data

An RES is a group of seismic events exhibiting nearly identical waveforms, magnitudes, and source locations. The magnitude and recurrence interval of the RES are sensitive to the loading rate, which provides useful information about how a fault creeps at depth (Beeler et al., 2001; K. H. Chen et al., 2007; T. Chen & Lapusta, 2009; Igarashi et al., 2003; Nadeau et al., 1995; Nadeau & Johnson, 1998; Sammis, 2001). Using the broadband seismic data recorded by the Broadband Array in Taiwan for Seismology (BATS, 1996), Y. Chen et al. (2020) identified 73 M2.3–4.6 RESs in the Chihshang fault with a mean focal depth of 16.4 km from 2000 to 2011. To be comparable with the InSAR and GPS data, we consider only the 36 RESs active during the study period of 2007–2011. They can be classified into a quasi-periodic type and an aperiodic type based on the covariance (COV) in the recurrence time (T_r) (K. H. Chen, Nadeau, & Rau, 2008). Given that the later type is likely associated with nearby moderate to large earthquakes, the quasi-periodic type (COV in T_r smaller than 0.5) is believed to better represent the inter-seismic slip rate over a relatively long timescale (Igarashi et al., 2003). Thus, out of the 36 RESs, seventeen quasi-periodic RESs composed of 65 repeating events are used for the following inversion.

3.3.1. RES-Derived Slip Estimates

An RES is the result of a re-rupture of the same patch of a fault that is driven to failure by continuous loading from the surrounding creeping area (e.g., T. Chen & Lapusta, 2009; Uchida & Bürgmann, 2019). The averaged recurrence time of repeating events in a quasi-periodic RES reflects the local creep rate in the immediate surrounding (Nadeau & Johnson, 1998; Nadeau & McEvilly, 1999). Therefore, cumulative slip of events from many RESs in a large region results from the averaged loading rate on the whole fault, while the cumulative slip of events in a RES corresponds to the aseismic slip history just around the RES patch. The local creep rate represents the loading condition in the immediate surroundings of an RES, which will be embedded in the inversion of inter-seismic slip rate of this study.

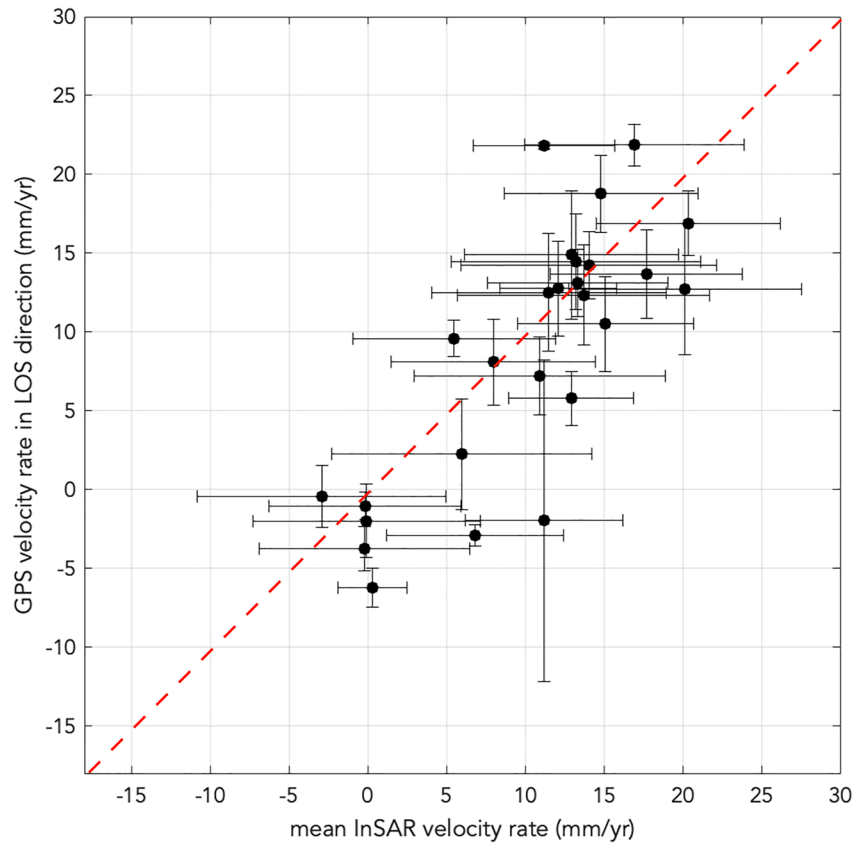


Figure 4. The comparison between mean synthetic aperture radar Interferometry (InSAR) data and Global Positioning System (GPS) data at each GPS site (locations shown in Figure 2a). Vertical and horizontal lines indicate the uncertainties of the measurements. The uncertainties for GPS and InSAR are obtained using bootstrap algorithm and standard error, respectively. Please see Sections 3.1 and 3.2 for details. The black dashed line represents a 1:1 relationship.

Assuming that the averaged aseismic fault slip is equal to the geodetically inferred fault slip rate (\dot{d}), then cumulative moment release ($\sum M_{0i}$) smoothed over the duration (T) of a given repeating sequence can be used to obtain the rupture area (A^{seq}), as shown by Equation 2. Note that i represents the i th event in a sequence.

$$A^{\text{seq}} = \frac{\dot{M}_0}{\mu \dot{d}} = \frac{\sum M_{0i}}{T \mu \dot{d}}. \quad (2)$$

Here \dot{M}_0 represents the average moment rate over duration T of a given RES, μ indicates the shear modulus. The seismic moment (M_{0i}) for each repeating event in this sequence can be obtained from:

$$M_{0i} = 1.5 \times 10^{(M_w + 9.1)}, \quad (3)$$

where M_w is the moment magnitude (Hanks & Kanamori, 1979). Now we treat the average rupture area for the sequence (A^{seq}) as the presentation of individual rupture area A_i . The slip (d_i) of individual repeating events can be inferred by:

$$d_i = \frac{M_{0i}}{\mu A_i} \quad (4)$$

For an individual sequence, the cumulative slip over the preceding recurrence interval (Tr) provides the slip rate measurement, as listed in Equation 5.

$$\dot{d}^{\text{seq}} = \sum_{i=2}^N d_i / \sum_{j=1}^{N-1} T_r(i), \quad (5)$$

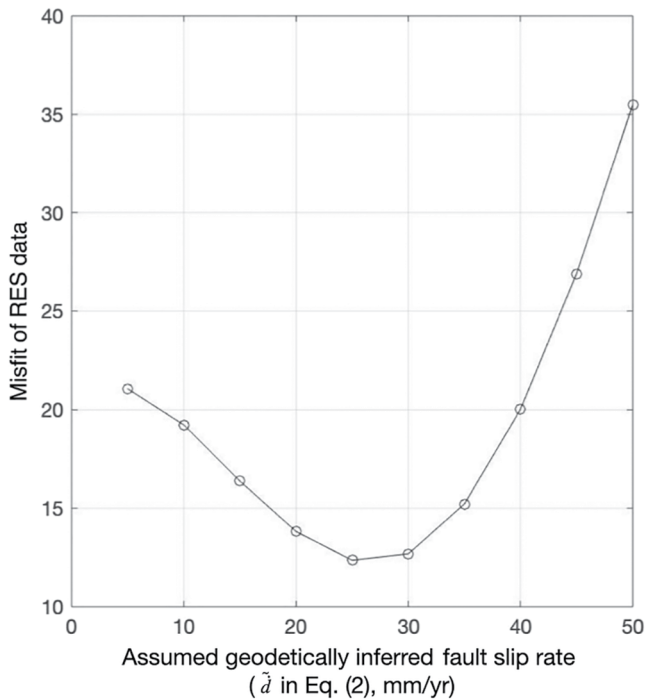


Figure 5. The misfit between the local creep rate inferred from the assumed fault slip rate and inverted inter-seismic slip rate as a function of the assumed fault slip rate in Equation 1. The optimal fault slip rate (25 mm/year) corresponds to the smallest misfit.

where N is the number of events in a sequence, Tr is the recurrence interval, i refers to individual event and j refers to individual recurrence interval. With such a calculation, the cumulative slip versus time can be formulated for the estimates of local creep rate (\dot{d}^{seq}) that represents the local creep condition in the immediate surrounding of a RES. The estimates of \dot{d}^{seq} at each RES location will be embedded in the joint inversion with GPS and InSAR data, to obtain the inter-seismic slip rate model. The inversion method will be addressed in Section 4.2.

Note that in Equations 2 and 5, the recurrence intervals and seismic moments are the key parameters that control the local creep rate. In this study, however, the problematic seismic signals with clocking errors and large noise level may lead to incomplete RESs catalog (K. H. Chen, Nadeau, & Rau, 2008; Y. Chen et al., 2020), which likely results in underestimation of the local creep rate. To avoid the possible \dot{d}^{seq} uncertainties introduced by missing repeating events, only the quasi-periodic RESs are adopted in this study. That says, the slip rate measurement is regarded as reliable for a sequence with a regular recurrence interval. To do so, only seventeen quasi-periodic sequences were used in the following analysis.

3.3.2. Empirical Relationship Between Slip and Moment

According to Equation 4, the slip for each repeating event (d_i) strongly depends on the choice of the assumed fault slip rate \dot{d} . In practice, the \dot{d} can be inferred from geodetic measurements (directly at the fault surface or indirectly with slip inversion). Here, we adopted the fault slip rate \dot{d} of 25 mm/year, which is chosen as the smallest misfit from a range of \dot{d} values in order to minimize the residual between the local creep rate using the assumed \dot{d} (Equation 2) and the inverted slip rate from joint inversion of RES, GPS and InSAR (Figure 5). The misfit is represented using the reduced chi-square statistic

($\chi^2_{red} = \frac{\sqrt{(\text{residual} / \text{uncertainty})}}{\text{number of data}}$). The inversion procedure will be introduced in Section 4.2.

To simplify the calculations in Equations 2–5, a scaling law between slip (d_i) and seismic moment (M_0) is usually inferred in a given study area (K. H. Chen et al., 2007; Y. Chen et al., 2020; Khoshmanesh et al., 2015; Nadeau & Johnson, 1998; Nadeau & McEvilly, 2004; Uchida et al., 2003)

$$\log d_i = \alpha + \beta \log M_0, \quad (6)$$

where d_i of the repeating event is proportional to the seismic moment M_0 , and α and β are fitting constants. Using the local creep rate derived from fault slip rate of 25 mm/year, we are able to invert the final estimate of inter-seismic slip rate on the fault including each RES site, using the RES, GPS and InSAR data. Here we attempt to examine the fitting constants α and β and discuss if there exists a regional difference. As shown by the d_i versus M_0 relationship in Figure S2 in Supporting Information S1, the 17 RESs yield $\alpha = -2.72$ and $\beta = 0.18$. By applying Equation 6 to infer the slip of an individual event, we summed the slips and divided by the time span of each RES to obtain the local creep rate.

Other than the scaling law in Equation 6, two other models commonly used to infer the slip of small earthquakes include (a) the standard crack model and (b) Beeler's model (Beeler et al., 2001). The standard crack model assumes that the slip accommodated at the location of RES is entirely seismic (Eshelby, 1957; Kanamori & Anderson, 1975). The slip can be determined by

$$d = \frac{M_0}{\pi \mu a^2}, \quad (7)$$

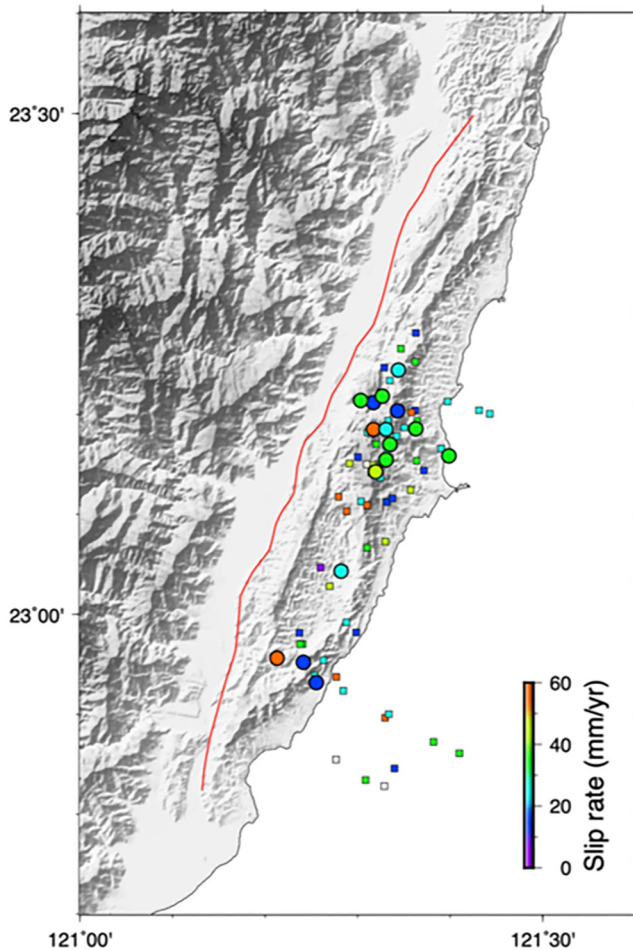


Figure 6. Spatial distribution of seventeen quasi-periodic repeating earthquake sequences composed of 65 events identified by Y. Chen et al. (2020). Circles indicate the quasi-periodic sequences used in this study, while squares indicate aperiodic sequences, color coded by the slip rates inferred from Equation 5.

where a indicates the rupture length which is computed by $a = (M_o / \Delta\sigma \times 7/16)^{1/3}$, μ is the rigidity, and $\Delta\sigma$ is the stress drop. Beeler's model (Beeler et al., 2001) on the other hand, assumes that both seismic and aseismic slip has been accommodating at the location of RES. The slip of an event in Beeler's model thus could be expressed as:

$$d = T_r V_L = \Delta\sigma \left[\frac{1}{1.81\mu} \left(\frac{M_o}{\Delta\sigma} \right)^{\frac{1}{3}} + \frac{1}{C} \right], \quad (8)$$

where T_r indicates the recurrence interval, V_L indicates the loading condition, C indicates the strain-hardening coefficient. Figure S3 in Supporting Information S1 shows the best fit of the observed T_r and M_o with different stress drop assumptions. By assuming $V_L = 2.5$ cm/year, the stress drop and C are chosen as 3 and 0.6 MPa/cm to better fit the observation of this study, while $V_L = 4.4$ cm/year, the stress drop and C are 10 and 1.1 MPa/cm, respectively. The C inferred here is consistent with the range obtained in northern Japan (Igarashi et al., 2003; Mavrommatis et al., 2015). When the slips inferred from standard model and Beeler's model are plotted against M_o , to compare with the observed d - M_o relationship in Figure S4 in Supporting Information S1, we found that the Beeler's model with the assumption of $V_L = 4.4$ cm/year, $\Delta\sigma = 10$ MPa (red line) and $V_L = 2.5$ cm/year, $\Delta\sigma = 3$ MPa (blue line with crosses). The standard model however, underestimates the slip, as revealed by two yellow lines in Figure S4 in Supporting Information S1. Such comparison suggests that the slip estimates from Equations 1 to 5 can be supported by Beeler's model and that the slip accommodated at the location of repeater should be both seismic and aseismic. Note that to have crack model fit into the observed trend, the high stress drops up to 100 MPa is needed, as denoted by purple line in Figure S4 in Supporting Information S1.

If the RES reveals perfectly periodic recurrence with the same magnitude, using the seismic moment to infer d_i in Equation 6 will give the same value as the d_i in Equation 4, which requires the duration and moment release rate of a sequence. However, in some cases the slip values from Equations 4 to 6 do not agree owing to fluctuation of the seismic moment and recurrence time of events in a sequence. The advantage of using Equation 6 is that it can be applied to the aperiodic RES but Equation 4 cannot. Therefore, in order to be potentially useful for the larger RESs data set, the refined $d - M_o$ relationship

from the seventeen quasi-periodic RESs is adopted for an estimate of slip for each repeating event. The colored circles in Figure 6 reveal the inferred slip rates of individual quasi-periodic RESs for the following joint inversion; The resulting slip rates have an average value of 30.7 mm/year with a standard deviation of 2.3 mm/year. The aperiodic RES (colored squares) however, reveals larger range of slip rates from 7 to 73 mm/year that may be associated the temporal fluctuation in local loading condition, which is not used in the following joint inversion.

4. Inversion Procedure

4.1. Fault Geometry

Based on the termination of the seismicity associated with the Chihshang fault, the north end of the fault is located at a latitude of 23.5°N. This boundary is also consistent with the discontinuity in the InSAR displacement field (Figure 3a). Note that this fault length is actually longer than the surface rupture during the 1951 H-T earthquake sequence (Shyu et al., 2005). The fault width is constrained by the hypocenters of the aftershocks following the 2003 M_w 6.8 Chengkung event and 2022 M_w 6.7 event shown in Figure S5 in Supporting Information S1, which reveals the depth range of the aftershocks from 0 to 29 km. Note that below the seismogenic zone at depths of 29–34 km where it is mostly freely creeping, the fault is able to simulate the long-term relative block motion. At the deepest zone, the slip rate is expected to be equivalent to the long-term slip rate. However, the lack of

Table 2
Fault Parameters Considered in This Study

	Chihshang fault		Central range fault	
	Depth range	Dip angle	Depth range	Dip angle
Shallow layer (grid: 1 × 1 km)	0–5 km	64°	0–5 km	60°
Middle layer (grid: 2 × 2 km)	5–29 km	44°	5–19 km	60°
Deep layer (grid: 4 × 4 km)	29–34 km	2°	19–20 km	2°
Strike	22°		201°	
Tectonic vector (rake)	145° (75°)		325° (75°)	
Fault length	85 km		85 km	
Fault width	54 km		22 km	
Deep creep rate (at deep layer)	40 mm/year		13 mm/year	

seismicity here fails to provide constraint on the fault geometry. To establish how the geometry of the fault below 29 km changes the slip rate variation in space, a sensitivity test was conducted and will be described in Section 5.1.

The above constraints lead to an along-strike fault length of 79 km and an along-dip fault width of 45 km. In our model, the fault plane is discretized into 1,932 small triangular fault patches with an average area of 3.2 km². The computation grid sizes on the fault plane are set to be 1 × 1 km, 2 × 2 km, and 4 × 4 km for the shallow portion (<5 km), the middle portion (5–29 km), and the deeper portion (29–34 km) of the fault, respectively. The fault parameters for the Chihshang fault are listed in Table 2.

4.2. Method for Joint Inversion

Using the fault model described above, we conducted static inversion using the velocity from GPS, InSAR, and RES. The forward matrix of joint inversion is expressed as:

$$\begin{bmatrix} d_{\text{GPS}} \\ d_{\text{InSAR}} \\ d_{\text{RES}} \end{bmatrix} = \begin{bmatrix} G_{\text{GPS}} & G_{\text{vector}} & 0 \\ G_{\text{InSAR}} & 0 & G_{\text{ramp}} \\ G_{\text{RES}} & 0 & 0 \end{bmatrix} \begin{bmatrix} m_{\text{slip}} + m_{\text{creep}} \\ m_{\text{vector}} \\ m_{\text{ramp}} \end{bmatrix}, \quad (9)$$

where d_{GPS} (black arrows in Figure 2a), d_{RES} and d_{InSAR} represent the observed velocity from GPS, RES, and InSAR, respectively. G_{GPS} and G_{InSAR} represent the Green's functions for GPS and InSAR, which were computed from an elastic half-space dislocation solution (Okada, 1992). G_{vector} indicates a designed identity matrix that was used to model the constant 2-D vector (eastward and northward motions) of m_{vector} (blue arrows in Figure 2a) to approximate the relative motion between the CeR block and the Costal Range block. G_{ramp} represents a linear ramp, controlled by the parameters in m_{ramp} , that was used to remove the residual orbital errors and adjust by a constant InSAR to match GPS data. However, since consistency between GPS and InSAR measurements is good enough (Figure 4), no adjustment was needed for the InSAR measurement. That is, G_{ramp} and m_{ramp} is assumed to be zero and neglected in the inversion process. G_{RES} represents the Green's function for RES that was used for assigning RES slips into fault patches. In practice, each RES slip was assigned to the closest single fault patch. Finally, m_{slip} represents the data prediction in each data set.

We followed the inversion method of Radiguet et al. (2011), where the least-squares formulation of Tarantola (2005) is applied for linear problems. The slip direction (rake) was fixed during the inversion. To determine the most representative rakes in each fault patch, the procedures are as follows: (a) Consider a unique “tectonic vector” as the projection of rake onto the mapview and counted counterclockwise from the East, which takes both strike and rake into account; (b) Applying the InSAR and GPS inversions using the selected range of tectonic vector; (c) Plotting normalized chi-square to obtain lowest misfit as the optimal value. The tectonic vector corresponding the lowest misfit goes to 145°, which is shown in Figure S6 in Supporting Information S1. Using the projection of the selected tectonic vector, the various strikes in each fault patch (details about fault geometry please see Section 4.1) lead to various rakes applied in the following inversion.

We also adopted a positivity constraint to fix the slip along the direction of motion to avoid any unrealistic slip values. The cost function for the inversion is:

$$S(m) = (Gm - d)^T C_d^{-1} (Gm - d) + (m - m_0)^T C_m^{-1} (m - m_0), \quad (10)$$

where the first term represents the fit to the data, in which the data covariance matrix is a diagonal matrix (covariances neglected) $C_d(j, j) = (w_j \sigma_d(j))^2$ associated with the data uncertainties (σ_d) and the weighting (w_j) between different data sets. The second term is the proximity to the initial model (here we set it to be zero slip), while C_m represents the model covariance matrix, which includes spatial smoothing. The elements of the covariance matrix $C_m(k, l)$ between the two sub-fault patches k and l with distance $d(k, l)$ are given by:

$$C_m(k, l) = \left(\sigma_m \frac{\lambda_0}{\lambda} \right)^2 e^{\left(\frac{-d(k, l)}{\lambda} \right)}, \quad (11)$$

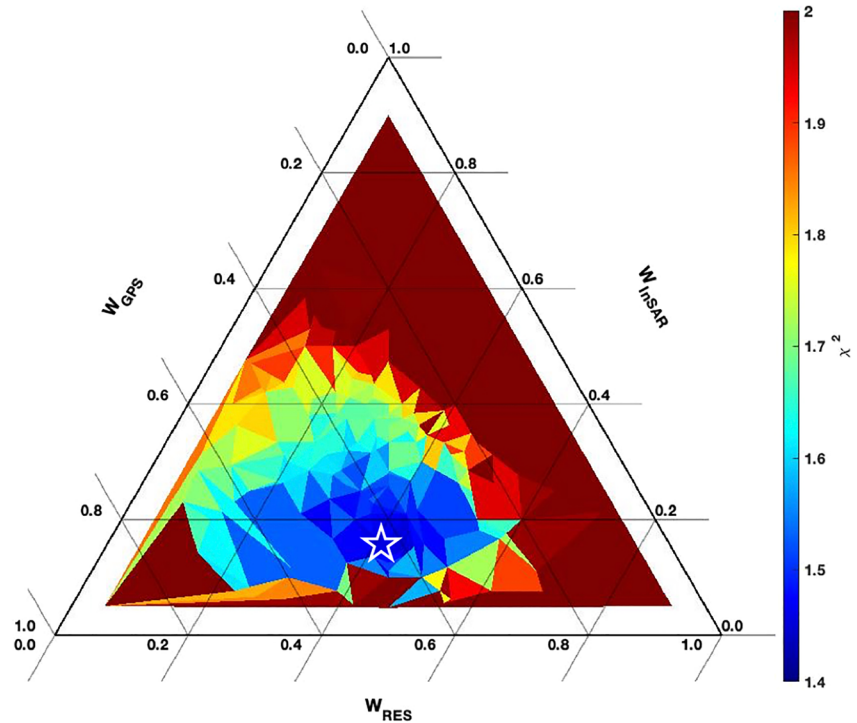


Figure 7. Ternary diagram with each of the three apexes representing a composition of Global Positioning System (GPS) weighting, synthetic aperture radar Interferometry (InSAR) weighting, and repeating earthquake sequence (RES) weighting. Color is coded by the resulting reduced chi-square. The white star indicates the optimal weighting values of w_{GPS} , w_{InSAR} , and w_{RES} as 0.4, 0.45, and 0.15, respectively, used in the inversion.

where λ is a correlation length and λ_0 is a reference length for the square root of the mean area for the sub-fault patches. σ_m is the a priori standard deviation of model parameters, which corresponds to a damping parameter. The optimal values of σ_m , λ , and w_i are determined from the trade-off between slip roughness and the goodness of fit to the data (reduced chi-square statistic). As shown in Figure S7a in Supporting Information S1, we explored a large range of damping values σ_m for a fixed correlation length $\lambda = 40$ km, and an optimal value of $\sigma_m = 10^3$ mm (green circle) was selected as a best compromise between model roughness and data misfit through the L curve criterion (Hansen, 1992). We also investigated the sensitivity of λ values in Figure S7b in Supporting Information S1. With a fixed $\sigma_m = 10^3$ mm, the optimal $\lambda = 40$ km was chosen to represent the termination of the dramatic reduction of chi-square. Note that these tests were performed without RES data in order to reduce the computation time. The weighting (w_i) of individual data sets is selected in a range of 0.01–1 for the grid search. Here we consider the same weighing in space for each data set. As shown in Figure 7, in order to achieve the smallest residual represented by the reduced chi-square, the optimal weightings for GPS (w_{GPS}), InSAR (w_{InSAR}), and RES (w_{RES}) were chosen as 0.40, 0.45, and 0.15, respectively.

5. Inversion Results

5.1. Spatial Variation of Slip Rates

After applying the above parameters selected by chi-square statistics, the GPS, InSAR, and RES data sets were used to invert for the inter-seismic slip of the Chihshang fault. The resulting slip model in Figure 8a shows that the shallow portion of the fault (above 20 km depth, denoted by the blue dashed line) has higher inter-seismic slip rate than the deeper portion from 20 to 29 km. The deeper zone below 20 km depth is characterized by lower slip rates and can be roughly divided into two zones, as separated by the white dashed line in Figure 8a; The southern half tends to have lower slip rate comparing with the northern half. At the deepest part (29–34 km), the slip rate was approximated by the maximum geodetic inferred slip rate by Thomas et al. (2014). The deepest zone plays a key role in accounting for the long-term slip rate. Since the geometry of the fault is not well characterized at the greater depths, a sensitivity test was performed to assess the impact of fault geometry and fault extension at depth

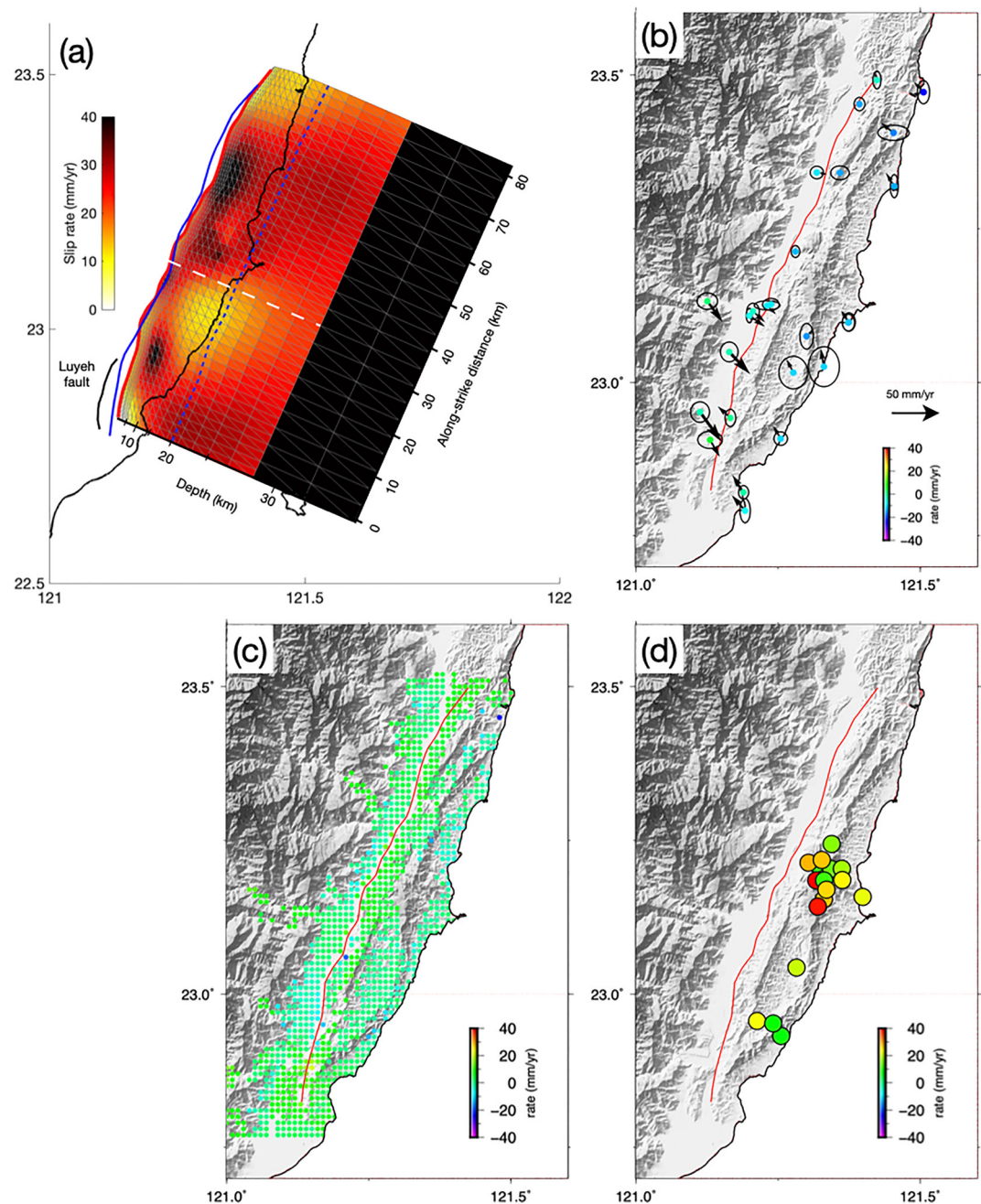


Figure 8. (a) Map of the inter-seismic slip obtained by the joint inversion. The blue dashed line indicates the approximately depth of 20 km. The white dashed line represents the boundary between the locked zone and creeping zone from depths 20–29 km. The red and blue solid lines indicate the fault trace of the Chihshang fault and Central Range fault, respectively. (b) Global Positioning System (GPS) residuals from the inversion with associated error ellipses. The circles represent the GPS stations and color indicates the residual from the vertical component. (c) Synthetic aperture radar Interferometry line-of-sight velocity residuals. Each circle represents a grid cell as in Figure 2b. (d) Residuals of slip derived from repeating sequence. The circles represent a repeating sequence as in Figure 6.

on the spatial variation of slip rate. This is shown in Figure S8a in Supporting Information S1, where the tested fault models have different dip angles (5° and 20°) and widths below the depth of 29 km (bottom depth ranging from 30 to 37 km). The resulting slip rates are averaged over depth and are shown in Figure S8b in Supporting Information S1. The along-strike variation of slip rates appears to be limited for the different geometries tested here, suggesting that the fault geometry below a depth of 29 km does not have a strong influence on the magnitude

of the inferred slip rate. We therefore, adopted the same dip-angle at the depth of 29 km and considered the maximum inverted slip rate (40 mm/year) at the deepest zone of 29–34 km as the initial condition in the kinematic fault model (e.g., Ching et al., 2007; Hsu et al., 2009).

The residuals between the observation and model for GPS, InSAR, and RES are shown in Figures 8b–8d. The residual of the GPS horizontal measurement falls in the range 1.5–10.3 mm/year to the north of 23.1°N and 5.0–20.3 mm/year to the south of 23.1°N (Figure 8b); for InSAR the misfits are 4.7 and 8.5 mm/year for the northern and southern segments, respectively (Figure 8c). The larger residuals in the south are likely the result of a more complex tectonic setting not accounted for in the model, in particular the partitioning of the deformation between the Chihshang fault and another structure, namely the Luyeh fault (the black line in Figure 8a). The misfit for the RES data is 7.1 mm/year (Figure 8d), where the relatively large residual is found to be associated with large coefficient of variation in recurrence interval (COV_{Tr}) for RESs. This can be seen in Figure S9 in Supporting Information S1 where greater than 10 mm/year residuals correspond to $COV_{Tr} > 0.30$, suggesting that the regular occurrence of an RES plays an important role in the reliability of the slip rate estimates.

The spatial variation of inter-seismic slip behavior is further established in Figure 9a, where the slip rates in various depth ranges are averaged for a given along-strike distance. There exists similar slip rate variation for all depth ranges—three peaks at the along-strike distance of 15, 40, and 55 km. The only exception is observed at the shallowest depth (<5 km, blue line), which shows the peaks at distance of 30 and 55 km with strong along-strike variations. In general, the shallow depths (5–10 km, light blue line) exhibit highest slip rates (up to 42 mm/year); At greater depths (20–29 km), the maximum slip rate reaches only 30 mm/year with much smoother variation along strike; The transition likely occurs at a depth of 10–20 km, where the high slip rate occupies the middle of the fault (distance of ~40 km in Figure 9a). To the south (distance of 10–20 km in Figure 9a), there exists significant depth dependency: at depths greater than 10 km the slip rate is low (<20 mm/year), while at shallow depths (<10 km) there is a localized high slip rate. To the north (distance of 50–80 km), the slip rates at various depths show similar bumps around the distance of 55 km, indicating weaker depth dependency.

5.2. Inter-Seismic Fault Coupling

Given that the long-term motion of the CoR with respect to the CeR is not well constrained in the literature, the inter-seismic coupling (ISC) here is obtained from the assumed deep creep rate (40 mm/year at depths below 29 km in Figure 8a), as shown in Equation 12 below. The selection of 40 mm/year is self-consistent with our model and close to the one inferred by Thomas et al. (2014) using another approach.

$$ISC = 1 - V_{int}/V_{longterm}, \quad (12)$$

where V_{int} and $V_{longterm}$ represent the modeled inter-seismic slip rate and maximum geodetic inferred long-term slip rate, respectively. An ISC of 1 describes a fully locked patch, while $ISC \approx 0$ describes a patch creeping at the long-term slip rate. The ISC resulting from the inter-seismic slip map (Figure 8a) is shown in Figure 9b. The co-seismic slip area of the 2003 M_w 6.8 Chengkung earthquake (pink contour) is found to be centered at a high coupling ratio, while the peak post-seismic slip (450 mm as denoted by the center of the green contour) occurred in a shallower zone (0–5 km), which has been previously documented as velocity-strengthening friction (H. Y. Chen et al., 2006; J.-C. Lee et al., 2006), and be penetrated into the deeper co-seismic slip zone. On 23 March 2022, a M_w 6.7 earthquake struck along the northmost segment of the Chihshang fault, as indicated by the cyan star in Figure 9b. The co-seismic slip inverted by seismic data and GPS (blue contour) is distributed at the deeper part of the northmost segment (Hsu et al., 2009; Thomas et al., 2014), which seems to be terminated around where the RES and swarm events occurred (Peng et al., 2021). The coupling ratio in the source area of the 2022 M_w 6.7 Yuli event is generally higher than average. Despite the resolution of our coupling model being relatively low at the edge of the fault (along-strike distances <5 km and >70 km), the correlation of the recent earthquake and high coupling ratio confirms that the northmost segment is likely strongly coupled.

Numerical and analytical studies and laboratory experiments suggest that RESs are formed on a small rupture surface (asperity) surrounded by velocity-strengthening areas (Beeler et al., 2001; T. Chen & Lapusta, 2019; Johnson & Nadeau, 2002) and thus are commonly regarded as indicators for aseismic slip. Earthquake swarms, although their mechanism is still not perfectly understood, are also considered to be related to aseismic slip (Ikari et al., 2013; Kubo & Nishikawa, 2020; Wang & Bilek, 2014). From the basic interpretation of ISC, aseismic transients are likely to occur on or near the low coupling areas. Figure 9b compares our ISC map with the hypocenter of $M \geq 3$ earthquake swarms (green circles, Peng et al., 2021) and $M \geq 2$ RESs (blue circles, Y. Chen et al., 2020). There is a strong

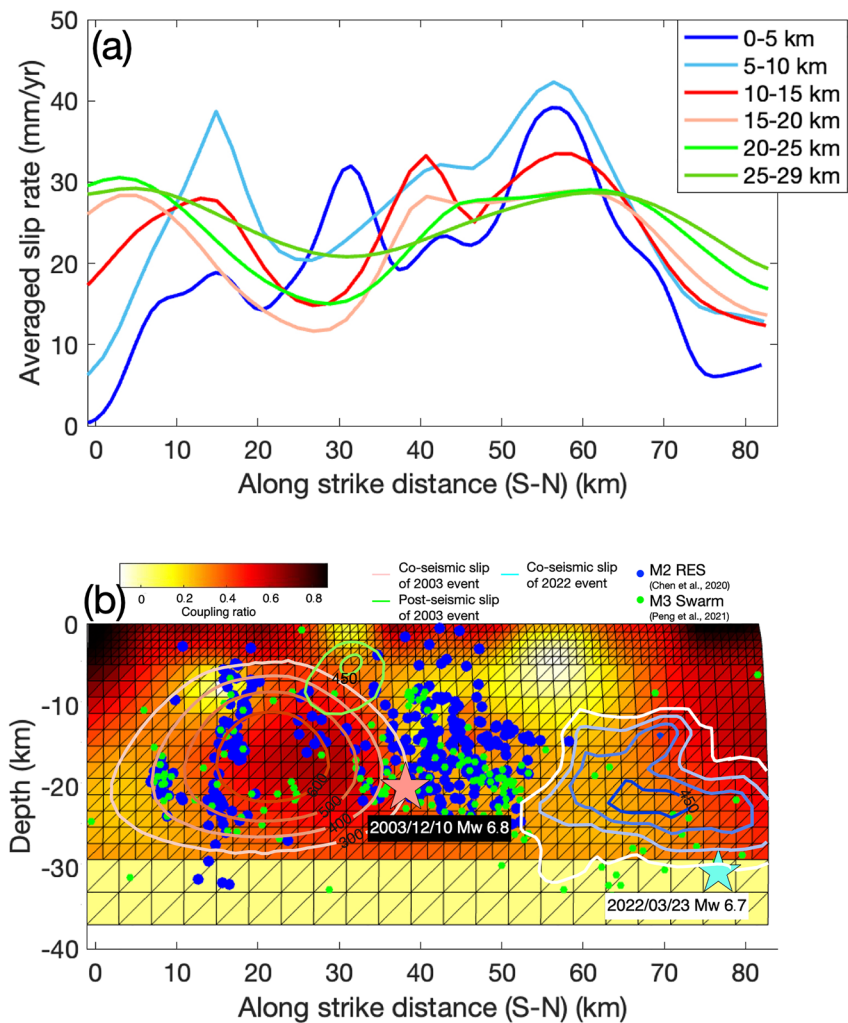


Figure 9. (a) Along-strike variation of slip rate in our best-fitting kinematic model. Each line represents the average slip rate with corresponding depth range. The along-strike distance corresponds to the cross-section in Figure 8a. (b) Coupling ratio on the fault plane. Pink and green contours indicate the co-seismic slip and the post-seismic slip of the 2003 M_w 6.8 Chengkung earthquake respectively, from Hsu et al. (2009). The cyan contours indicate the co-seismic slip of the 2022 M_w 6.7 Yuli earthquake. Here only slips over 70% of the maximum value (denoted by the number in the center of contours) are plotted at contours intervals of 100 mm. The blue circles indicate the $M \geq 2$ repeating events identified by Y. Chen et al. (2020). Green circles indicate the $M \geq 3$ swarm events identified by Peng et al. (2021). Pink and cyan stars indicate respectively the hypocenters of the 2003 M_w 6.8 and 2022 M_w 6.7 mainshocks.

overlap between the locations of RESs and earthquake swarms (indicated by blue and green circles, respectively, in Figure 9b), and both occur mainly around the co-seismic slip zone of the 2003 Chengkung event. Based on quantitative analysis by Peng et al. (2021), only 14% of RESs are located outside a 5 km distance from the swarms. Both these seismic activities are found to coincide with a low coupling ratio, suggesting an environment of aseismic creep. The areas of co-seismic slip during the 2003 M_w 6.8 Chengkung event and 2022 M_w 6.7 Yuli event coincide with the relatively large coupling ratio, as indicated by the pink and blue contours in Figure 9b, respectively. The aseismic slip episodes appear to take place in the surroundings of the contours through the phenomena of RESs and earthquake swarms. The post-seismic area denoted by the green contour, however, coincides with a low coupling ratio and appears to be a transition zone separating the co-seismic slip area and the low coupling ratio area at shallow depth.

5.3. Seismicity Versus Coupling Model

The spatial variability of seismicity may result from differences in the mechanical properties of a fault. As seismicity is an intrinsically independent observation from the coupling measurement, the earthquake behavior is

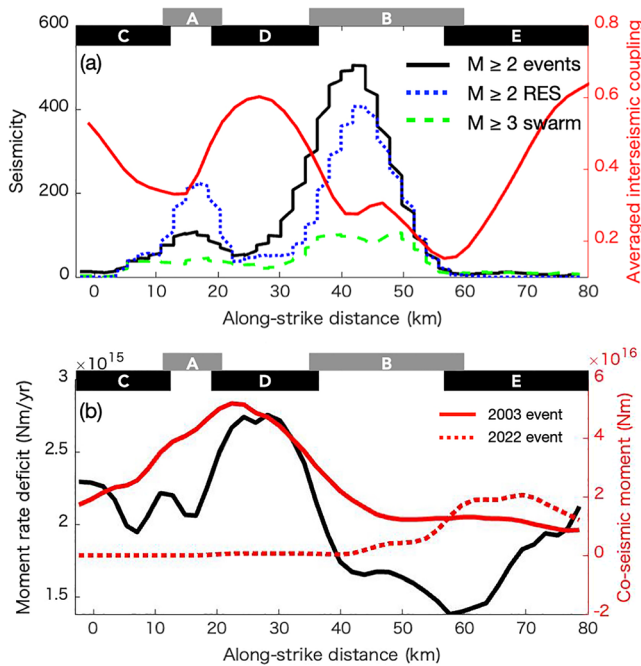


Figure 10. (a) Along-strike variation of seismicity, co-seismic slip, and the average coupling ratio at depths from 5 to 25 km on the Chihshang fault. The blue and green dashed lines represent respectively the number of $M \geq 2$ repeating events and number of $M \geq 3$ swarm events. The red solid line represents the average coupling ratio. The seismicity was determined by counting the events within a 5 km radius of the fault patch. (b) The comparison between the interseismic moment rate deficit and co-seismic moment from 2003 to 2022 events along the Chihshang fault at depths from 5 to 25 km. The black line represents the average moment rate deficit estimated by our inter-seismic slip model. The red solid line and red dashed line indicate the averaged co-seismic moment of the 2003 M_w 6.8 Chengkung event and 2022 M_w 6.7 Yuli event, respectively.

compared with the coupling model in Figure 10a. Based on different mechanical behaviors (detailed below), the Chihshang fault was separated into five regions along the strike from A to E. The ISC, $M \geq 2$ background seismicity, and $M \geq 2$ RESs and swarms were averaged over the depth range 5–25 km and at 1.25 km intervals of along-strike distance. The background seismicity (black line in Figure 10a) is mainly concentrated in areas A and B and is consistent with the distribution of $M \geq 2$ repeating earthquakes (dashed blue line in Figure 10a) and the $M \geq 3$ earthquake swarm (dashed green line in Figure 10a). The spatial variation of seismicity, however, shows an anti-correlation with that of the ISC (areas D and E). The moderate coupling in area C is likely mixed with the seismic activity on the close-by Luyeh fault (black line in Figure 8a) and thus does not precisely reflect the coupling behavior on the Chihshang fault. Note that the Luyeh fault hosted a M_w 6.2 event on 1 April 2006.

The inter-seismic moment rate deficit can be further obtained from $M_{\text{deficit}} = \mu \sum A_i \times V_{\text{longterm}} \times \text{ISC}$, where μ indicates the shear modulus, A_i indicates the area of fault patch i , and V_{longterm} indicates the maximum geodetically inferred long-term slip rate (40.1 mm/year). The total M_{deficit} is determined to be 2.71×10^{18} dyne-cm/year on the fault. The along-strike variation of M_{deficit} can be shown in Figure 10b, where the co-seismic slip seismic moments of the 2003 M_w 6.8 and 2022 M_w 6.7 earthquakes (red solid line and red dashed line, respectively) spanning areas D and E appear to coincide with the moment rate deficit pattern. That is, the energy accumulated over the study period 2007–2011 establishes that the deficit is mostly concentrated in area D. The moment rate deficit in this particular area was determined to be 2.27×10^{17} Nm/year, which is able to generate an M_w 6.8 event every 78.3 years. Given that the previous event occurred in 2003, we expect that the next M_w 6.8 event will return in 2081. The other locked area, area E, had been quiet for a long time but experienced an M_w 6.7 event in 2022. This area is capable of accumulating moment at a rate of 4.40×10^{17} Nm/year, equivalent to a return period of 28.6 years for the same magnitude event. However, there exists several uncertainties in the estimates of recurrence interval of the locked zones. First, the inferred inter-seismic slip rate in this study can

only represent the behavior during the study period, from 2007 to 2011. The understanding of temporal evolution in seismic versus aseismic slip will be needed to infer the seismic potential of the Chihshang fault. Second, the fault interaction between the LVF and CRF may alter the recurrence behavior of the Chihshang fault, this will be further addressed in Section 6.1.

The coupling model in Figure 9b can be further illustrated by the conceptual model in Figure 11. In a rate-state friction concept, frictional properties can be expressed by the size and spatial distribution of asperities that correspond to the value of ISC. The areas with low ISC but no seismic event are regarded as freely creeping. During the inter-seismic period, the freely creeping areas tend to accumulate and release stress aseismically, as denoted by the orange area in Figure 11. The strongly coupled area that is characterized by high ISC, on the other hand, corresponds to the large asperity. Such region is capable of accumulating strain and releasing most of the stress through $M \geq 6$ events, as indicated by gray areas in Figure 11 (Sammis, 2001; Scholz, 1998; Wesson & Nicholson, 1988), which corresponds to the co-seismic slip areas of the 2003 M_w 6.8 and 2022 M_w 6.7 events (contours in Figure 11). The highest ISC corresponds to strong coupling and relatively large co-seismic slip, as indicated by light yellow areas. In the region that exhibits low ISC, earthquakes mainly occur with smaller magnitude in a repeatable or clustered manner, which is denoted as partially creeping. As denoted by green areas with smaller gray circles, there exists small magnitude earthquakes and RESs embedded in a creeping fault. The green areas happen to separate the freely creeping (orange) and strongly coupled (light yellow and contoured) areas, which represent the gradual change in frictional properties from aseismic to seismic slip.

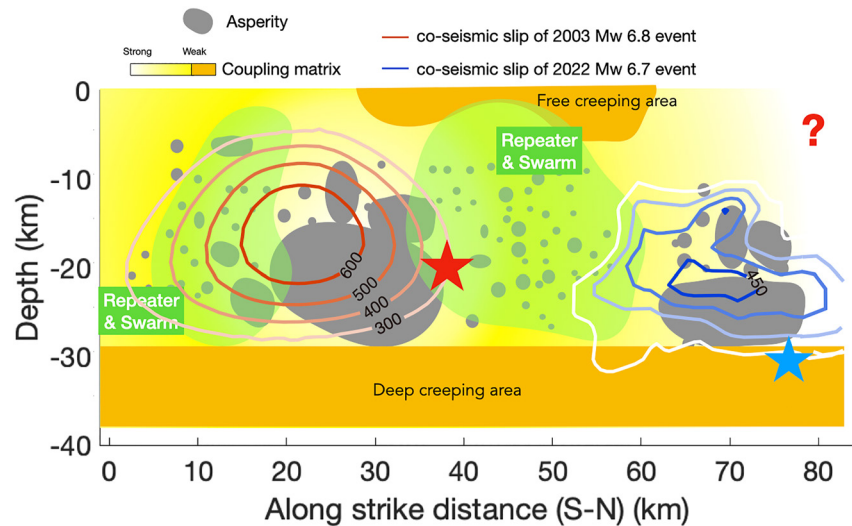


Figure 11. Conceptual model of the Chihshang fault based on the seismicity and inter-seismic slip model. In the general setting, the fault exhibits freely creeping behavior at the lowest depth (orange zones, depths of 29–37 km) and heterogeneous couplings from strongly coupled (white and yellow) to decoupled (orange) at higher depths (depths of 0–29 km). Two freely creeping zones at the shallower depth (0–10 km) are mainly characterized by low coupling ratio and reduced seismicity. Green areas represent a partially creeping area that is characterized by low coupling ratio and enhanced activity of repeating earthquake sequences and swarm events. Red and blue contours indicate the co-seismic slip of the 2003 M_w 6.8 Chengkung earthquake and the 2022 M_w 6.7 Yuli earthquake.

6. Discussion

6.1. Two-Fault Kinematic Model

Unlike the Chihshang fault where the fault geometry and surface slip rate has been precisely measured, the CRF in the south of 23.5° is less known and poorly constrained. The main reasons are the lack of geodetic data coverage in the mountain area (the west of CRF) and the infrequent earthquake activities. The west-dipping CRF characterized by ~1 cm/year long-term slip rate (Shyu et al., 2006) was suspected to be responsible for the historical M_L 7.3 Yuli event in the 1951 H-T sequence (Shyu et al., 2006, 2023) and had been quiet until 2022. The occurrence of M_w 6.5 and M_w 7.0 Guanshan-Chihshang earthquake sequence in September 2022 (S.-J. Lee et al., 2023) confirmed the capability of the CRF to produce powerful events. As shown in Figure S10 in Supporting Information S1, the two mainshocks and their aftershocks in this 2022 earthquake sequence are located underneath the eastern flank of the Central Range (CeR in Figure S10 in Supporting Information S1), separated from earthquakes on the east-dipping Chihshang fault. We next examine whether the consideration of CRF changes the inter-seismic slip model for the Chihshang fault, hereafter referred as “two-fault model.” The fault parameters of CRF were chosen using the available co-seismic slip model, focal mechanism, and aftershock distribution (the detailed description please see Text S1 in Supporting Information S1 and Table 2). In this two-fault model, we applied a positivity constraint (Radiguet et al., 2011) and fixed the tectonic vector of the LVF and CRF at 145° and 325°, respectively. Here the tectonic vector of the CRF is assumed to follow the opposite direction to the Chihshang fault (325°) in order to minimize the slip partitioning. With the various strikes, the rake of the CRF ranges from 61.2° to 95.0° with the mean value of 76.3°.

Same with the modeling parameters considered in the inversion in Section 3.2, here the smoothing parameter (λ) is assumed to be 40 km for both faults. Given that the geodetic measurements are mostly near fault trace, while the RES are not observed on the CRF, the along-dip variation of inter-seismic slip rate on CRF is not well constrained. This leads to a need for assuming the upper bound of the slip rate around 1.3 cm/year at the depth below 20 km as the maximum inter-seismic slip rate inferred by Shyu et al. (2006). The modeling parameters of CRF are listed in Table 2. The resulting inter-seismic slip model is shown in Figure 12a, where the CRF appears to slip with mean slip rate of 3.2 mm/year at the depth of shallower than 19 km, where the maximum slip rate of 22.37 mm/year occurs near the southern end of the fault (along-strike distance of 0–10 km).

Note that the slip distribution of LVF using two-fault model in Figure 12a shows a nearly identical pattern with the single fault model in Figure 12b, especially at the depth shallower than 20 km. Comparing with the single-fault

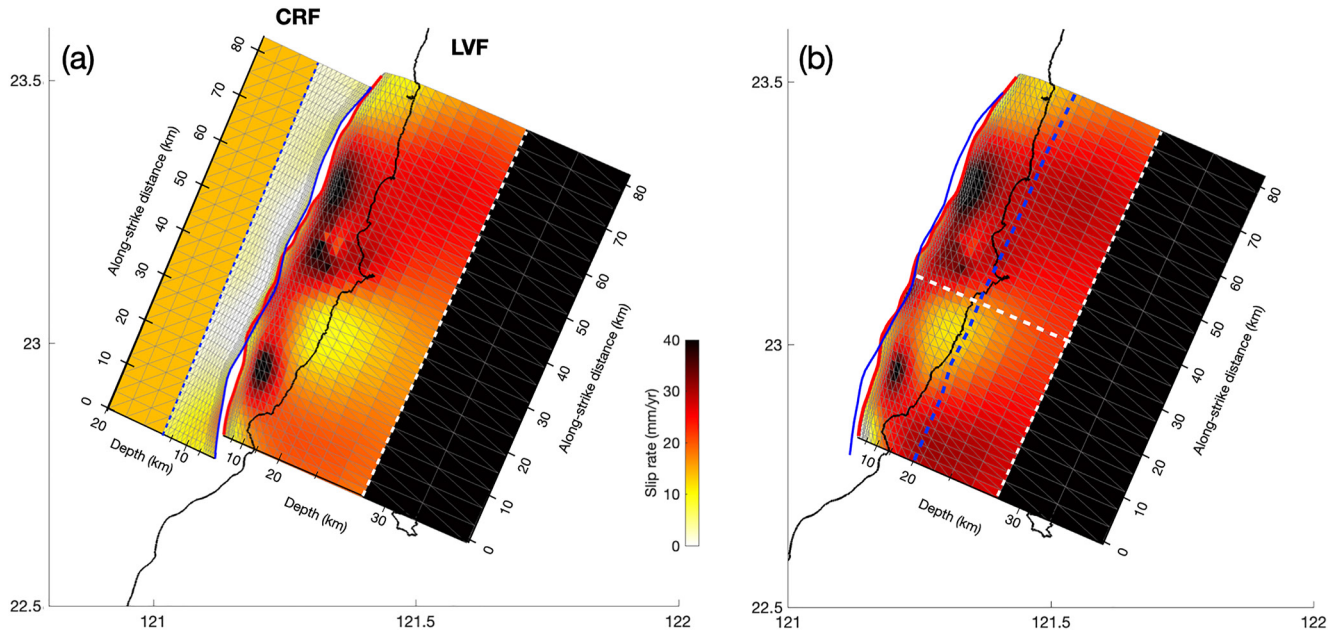


Figure 12. (a) Map of the inter-seismic slip of two-fault model obtained by the joint inversion. Blue and white dash line represent the 19 and 29 km depth of Central Range fault (CRF) and Chihshang fault, respectively. Below these depths, the faults are assumed to creep with a constant rate due to the lack of resolution for along-strike and along-dip distribution of slip behavior. The constant creep rates for the Chihshang fault and CRF are assumed to be 4.0 and 1.3 cm/year, respectively. (b) The inter-seismic slip model of one-fault model, the same with Figure 8a.

model, the two-fault model reveals slightly smaller slip rate at the greater depth below 20 km (difference smaller than 1 cm/year); the along-strike variation however, remains the same. The difference of the inverted slip rate on the Chihshang fault between the two fault models (hereafter referred as *Diff*) is shown in Figure S11 in Supporting Information S1. Comparing with the single fault model, the inverted slip rates on the Chihshang fault are reduced 2–10 mm/year at the depth below 20 km in two-faults model. The largest *Diff* (10.23 mm/year) occurs at southern, deep part of the fault (along-strike distance = 0–10 km, depth ~20 km). To confirm whether this large *Diff* is due to the model uncertainty, we next map the model uncertainty in each fault patch by applying different smoothing and damping parameters, λ and σ_m in Equation 11. Here we compute the standard deviation using the 16 slip rate estimates produced by $\lambda = 30$ –80 km and the 21 slip rate estimates produced by $\sigma_m = 10^{2.5} - 10^{3.5}$, which is shown in Figure S12 in Supporting Information S1. Note that the model uncertainty at the corner where the largest *Diff* occurs (Figure S11 in Supporting Information S1) is confined in a small range of 1–4 mm/year. The largest standard deviation, on the other hand, appears to occur at the patches characterized by extreme slip rates that changes significantly over different λ and smaller σ_m . This suggests that the large difference of the inferred slip rates between the two models likely reflects the real difference, which should be noted in the future study. Note that the interseismic moment rate deficit inferred from two-fault model is 2.43×10^{18} dyne-cm/year, roughly 10% smaller than the one inferred from single-fault model. The recurrence intervals for M_w 6.8 event in areas D and M_w 6.7 in area E of Figure 10 would be altered to 79.4 and 31.1 years, respectively, in the two-fault model.

To further confirm the source of model uncertainties, the residual can be also mapped into the individual observational data sets. As shown by Table S1 in Supporting Information S1, the residual in GPS horizontal component (Chi-square statistics) is found to reduce slightly from 13.5 to 11.1 mm/year using two-fault model, where the residual in other two data sets (InSAR and RES) only changes insignificantly. Note that the uncertainties in fault parameters chosen for the CRF here (Table 2) remains large. The reasons are: (a) The long-term slip rate at the bottom of the fault is only approximated by assuming that the 1951 M_L 7.3 and 2022 M_w 7.0 events ruptured the same fault, which is lack of geodetic constraint; (b) The fault geometry of CRF can be largely improved if the relocation and focal mechanisms determination of the aftershocks is performed. Consequently, the demonstration of two-fault model suggests that the contribution of the CRF in the kinematic modeling of the Chihshang fault is notable and potentially leads to the better understanding of the regional inter-seismic deformation, which requires further attention through better geodetic and seismic networks in the future.

6.2. Role of Repeating Earthquakes on Slip Inversion

RESs have been widely used as a simple creepmeter embedded in the fault (see the review article by Uchida & Bürgmann, 2019). However, there exists a long-standing debate about the applicability of the relationship between seismic moment (M_0) and RES slip (Equation 6). As the geodetically inferred mean fault slip rate (\dot{d} in Equation 2) represents the loading condition in the immediate surroundings of an RES, the slip (d_i in Equation 4) accumulated in the RES patch can thus be approximated by the fault slip rate (\dot{d}) multiplied by the total duration of the RES. The assumed fault slip rate plays a role in the determination of slip for an individual repeating event (d_i in Equation 4) and thus influences the d_i versus M_0 relation in Equation 6.

Y. Chen et al. (2020) examined how much the assumed \dot{d} (geodetically inferred slip rate) changes the constants α and β in Equation 6. They found that α increases with increasing \dot{d} while β remains unchanged. This suggests that, when a greater loading rate on the fault (\dot{d}) is considered, the inferred RES slip (d_i) increases too. The dependency of seismic moment on slip, however, remains the same under various loading rates. In their study, the surface creepmeter acts as a constraint for determining which \dot{d} is more reasonable for the regional slip rate estimate. As the individual slip of an RES is summed in time to infer the regional slip rate, they proposed the resulting regional slip rate from the RES be higher than the surface slip rate from a creepmeter. To meet such a requirement, $\dot{d} = 44$ mm/year was adopted.

In this study, we obtained a favorable \dot{d} via a better agreement with the jointly inverted slip rates (Figure 5). Based on the minimal residual between the assumed \dot{d} and chi-square in the joint inversion, the resulting optimal \dot{d} is 25 mm/year, which is approximately 1.7 times smaller than that used by Y. Chen et al. (2020). As in Y. Chen et al. (2020), the comparison with surface creepmeter data may not be sufficient to constrain the choice of \dot{d} . In addition to propose a better way for the decision of \dot{d} , some questions require our investigation: (a) how much difference does the choice of 44 or 25 mm/year cause in the inter-seismic slip model and (b) when the geodetic inversion is not available as in the study of Y. Chen et al. (2020), what might we misinterpret or miscalculate?

As shown in Figure S13 in Supporting Information S1, the fault slip rate of 25 mm/year (decided by the smallest residual shown in Figure 5) for RES analysis and 44 mm/year assumed in Y. Chen et al. (2020) lead to similar spatial characteristics but slightly different magnitudes of slip rate. The different outcomes of the inversions can be established by the along-strike variation of slip rates averaged over different depth ranges in Figure S14 in Supporting Information S1. Note that the inversions without RES data were also performed, as indicated by “geodetic inversion” (gray line), while the joint inversions with both geodetic and RES data are denoted by orange and blue lines in Figure S14 in Supporting Information S1. At shallow depths (0–10 km), the geodetic inversion (gray line) and two joint inversions with 44 and 25 mm/year local slip rates for RES data (blue and orange lines, respectively) reveal nearly identical patterns, indicating the consistency between the three inversions. At the depth of 10–20 km where the majority of RES are distributed, the difference between three inversions appears. The geodetic inversion (gray line) peaks at the along-strike distances of 8 and 60 km, which are significantly different from those for the joint inversions (blue and orange lines) at distance of 40 km. The largest difference between the two joint inversions is found to occur at distance of 40–50 km, coinciding with where the majority of RESs are distributed. When the high local slip rate (44 mm/year) is introduced into the inversion, the inferred slip rate at this RES-rich zone is up to 40 mm/year, while the inferred value is 32 mm/year under the low local slip rate (25 mm/year) assumption. Such difference is mainly contributed by the spatially clustered 12 RES in this distance range (40–50 km). This suggests that with the constraint by the geodetic data, the assumption of local slip rate tend to influence the area where a larger number of RES occupied, and the inferred slip rate is close to the assumed local slip rate. At the bottom of the seismogenic zone greater than 20 km depth where the RES are relatively small in number, the three inversions reveal similar variation along the strike, but the geodetic inversion alone generates a higher slip rate (gray line compared with the orange and blue lines in Figure S14 in Supporting Information S1). The joint inversions using two different local slip rates, however, reveal very similar magnitudes at this depth range. There exists large difference between the geodetic (gray line) and joint inversions (orange and blue lines) due to the limited resolution at greater depth.

Given that RES provides the spatial variation of slip rates relative to the assumed average (loading velocity), it is reasonable that the different assumption of fault slip rate does not change very much in the inverted inter-seismic slip rate variation in space except for the localized area where the largest number of RESs are distributed. This sensitivity test in Figure S14 in Supporting Information S1 suggests that the complexity of slip rate variation

in space can be enhanced when the RES data are considered in the inversion. The improvement is greatest at depths of more than 10 km, where the geodetic data alone starts to lose resolution and RES starts to increase the contribution. It also confirms that combining the geodetic observation and repeating earthquakes in a fault yields a finer understanding of slip rate behavior with depth.

7. Conclusions

We have evaluated a time-independent inter-seismic slip by combining geodetic data and seismic data. By taking advantage of RESs that mainly occurred below 10 km, we were able to increase the model resolution at depths below 10 km and establish the fine structure of the inter-seismic slip rate. Using geodetic and seismological data from 2007 to 2011, we demonstrated a correlation between the earthquake phenomena and the inferred coupling model. For regions exhibiting strong coupling ($ISC > 0.5$), earthquakes mainly occurred with a form of mainshock–aftershock sequence that agreed with the concentration of co-seismic slip for the two M6 mainshocks in 2003 and 2022. The regions showing weak coupling ($ISC < 0.5$) were confined to shallow depths above 10 km, where the inter-seismic slip rate was generally high with inactive seismicity. The inferred intermediate low coupling ratio ($ISC \approx 0.5$) establishes an extensive creeping area that coincides with the location of abundant repeating earthquakes and swarm events. In between the weak and strong coupling areas, there exists a transition zone that hosted the post-seismic slip following the 2003 M_w 6.8 earthquake. The strong along-strike and along-dip variations of the inter-seismic slip on the Chihshang fault led to the measurement of the inter-seismic deficit rate. We obtained the moment rate deficit for the areas where the 2003 and 2022 $M \geq 6$ events occurred to be 2.27×10^{17} and 4.40×10^{17} Nm/year, respectively, assuming a long-term slip rate of 40 mm/year. The locked area of the 2003 event is capable of generating the event with same magnitude every 78 years, whereas the area of the 2022 event has a return period of approximately 28 years. We also established the role of adjacent CeR fault in the inter-seismic modeling. The consideration of CeR fault in the two-fault model appears to have considerable influence in the kinematic modeling of the Chihshang fault. The inter-seismic moment rate deficit inferred from two-fault model is roughly 10% smaller than the one inferred from single-fault model, leading to slightly longer recurrence intervals for the 2003 and 2022 locked zones as 79 and 31 years, respectively. This suggests a need for pursuing a time-dependent kinematic model by considering both the LVF and CRF in the future.

Data Availability Statement

GNSS data used in this study is provided by the website <http://tgm.earth.sinica.edu.tw>. InSAR data is processed and provided by Champenois et al. (2012) and Thomas et al. (2014). Repeating earthquake data is attributed to Y. Chen et al. (2020) which benefited from the Central Weather Bureau Seismic Network (<http://gdms.cwb.gov.tw/index.php>) and Broadband Array in Taiwan for Seismology (BATS, 1996, <https://bats.earth.sinica.edu.tw/>). Figures were created through Matlab R2022b (The Mathworks Inc, 2022) and Generic Mapping Tools (GMT) version 5 (Wessel et al., 2013) licensed under LGPL version 3 or later, available at <https://www.generic-mapping-tools.org/>. Matlab scripts and processed data of GPS, InSAR and repeating earthquake sequence associated with this manuscript for the calculation of slip inversion are available at (Peng, 2023).

Acknowledgments

The authors acknowledge the support from CNRS (The CNRS IEA 2020 project LVF-Faultand in part by the Agence Nationale de la Recherche, Grant ANR-21-CE49-0021-01. A CC BY license is applied to the AAM arising from this submission, in accordance with the grant's open access conditions) and Taiwan MOST Grants 110-2927-I-003-502 and 111-2116-M-003-008-MY3. We wish to thank Nina Yunung Lin for the guidance of InSAR data processing and modeling at the early stage of this project. We wish to thank the anonymous reviewers, Associate Editor, and Editor for their valuable comments. We would like to thank Uni-edit (www.uni-edit.net) for editing and proofreading this manuscript.

References

- Angelier, J., Chu, H.-T., & Lee, J.-C. (1997). Shear concentration in a collision zone: Kinematics of the Chihshang Fault as revealed by outcrop-scale quantification of active faulting, Longitudinal Valley, eastern Taiwan. *Tectonophysics*, 274(1–3), 117–143. [https://doi.org/10.1016/S0040-1951\(96\)00301-0](https://doi.org/10.1016/S0040-1951(96)00301-0)
- BATS (Broadband Array in Taiwan for Seismology). (1996). [Dataset] Institute of Earth Sciences, Academia Sinica, Taiwan. Other/Seismic Network. <https://doi.org/10.7914/SN/TW>
- Beeler, N. M., Lockner, D. L., & Hickman, S. H. (2001). A simple stick-slip and creep-slip model for repeating earthquakes and its implication for microearthquakes at Parkfield. *Bulletin of the Seismological Society of America*, 91(6), 1797–1804. <https://doi.org/10.1785/0120000096>
- Bertiger, W., Bar-Sever, Y., Dorsey, A., Haines, B., Harvey, N., Hemberger, D., et al. (2020). GipsyX/RTGx, a new tool set for space geodetic operations and research. *Advances in Space Research*, 66(3), 469–489. <https://doi.org/10.1016/j.asr.2020.04.015>
- Bürgmann, R. (2018). The geophysics, geology and mechanics of slow fault slip. *Earth and Planetary Science Letters*, 495, 112–134. <https://doi.org/10.1016/j.epsl.2018.04.062>
- Bürgmann, R., Schmidt, D., Nadeau, R. M., d'Alessio, M., Fielding, E., Manaker, D., et al. (2000). Earthquake potential along the Northern Hayward Fault, California. *Science*, 289(5482), 1178–1182. <https://doi.org/10.1126/science.289.5482.1178>
- Champenois, J., Fruneau, B., Pathier, E., Deffontaines, B., Lin, K.-C., & Hu, J.-C. (2012). Monitoring of active tectonic deformations in the Longitudinal Valley (Eastern Taiwan) using persistent scatterer InSAR method with ALOS PALSAR data. *Earth and Planetary Science Letters*, 337–338, 144–155. <https://doi.org/10.1016/j.epsl.2012.05.025>

- Chen, H.-Y., Yu, S.-B., Kuo, L.-C., & Liu, C.-C. (2006). Coseismic and postseismic surface displacements of the 10 December 2003 (Mw 6.5) Chengkung, eastern Taiwan, earthquake. *Earth, Planets and Space*, 58(1), 5–21. <https://doi.org/10.1186/BF03351908>
- Chen, K. H., Nadeau, R., & Rau, R. J. (2008). Characteristic repeating earthquakes in an arc-continent collision boundary zone: The Chihshang fault of eastern Taiwan. *Earth and Planetary Science Letters*, 276(3–4), 262–272. <https://doi.org/10.1016/j.epsl.2008.09.021>
- Chen, K. H., Nadeau, R. M., & Rau, R.-J. (2007). Towards a universal rule on the recurrence interval scaling of repeating earthquakes? *Geophysical Research Letters*, 34(16), L16308. <https://doi.org/10.1029/2007GL030554>
- Chen, K. H., Rau, R.-J., & Hu, J.-C. (2009). Variability of repeating earthquake behavior along the Longitudinal Valley fault zone of eastern Taiwan. *Journal of Geophysical Research*, 114(B5), B05306. <https://doi.org/10.1029/2007JB005518>
- Chen, K. H., Toda, S., & Rau, R. J. (2008). A leaping, triggered sequence along a segmented fault: The 1951 ML 7.3 Hualien-Taitung earthquake sequence in eastern Taiwan. *Journal of Geophysical Research*, 113(B2), B02304. <https://doi.org/10.1029/2007JB005048>
- Chen, T., & Lapusta, N. (2009). Scaling of small repeating earthquakes explained by interaction of seismic and aseismic slip in a rate and state fault model: Simulations of repeating earthquakes. *Journal of Geophysical Research*, 114(B1), B01311. <https://doi.org/10.1029/2008JB005749>
- Chen, T., & Lapusta, N. (2019). On behaviour and scaling of small repeating earthquakes in rate and state fault models. *Geophysical Journal International*, 218(3), 2001–2018. <https://doi.org/10.1093/gji/ggz270>
- Chen, W.-S., Wu, Y.-M., Yang, H.-C., Yeh, P.-Y., Lai, Y.-X., Ke, M.-C., et al. (2020). Seismogenic structures of the collision-subduction zone in the eastern Taiwan. In *EGU General Assembly Conference Abstracts*, 4453.
- Chen, Y., Chen, K. H., Hu, J., & Lee, J. (2020). Probing the variation in aseismic slip behavior around an active suture zone: Observations of repeating earthquakes in Eastern Taiwan. *Journal of Geophysical Research: Solid Earth*, 125(5), e2019JB018561. <https://doi.org/10.1029/2019JB018561>
- Cheng, S.-N., Yeh, Y.-T., & Yu, M.-S. (1996). The 1951 Taitung earthquake in Taiwan. *Journal of the Geological Society of China-Taiwan*, 39, 267–286.
- Ching, K.-E., Rau, R.-J., & Zeng, Y. (2007). Coseismic source model of the 2003 Mw 6.8 Chengkung earthquake, Taiwan, determined from GPS measurements. *Journal of Geophysical Research*, 112(B6), B06422. <https://doi.org/10.1029/2006JB004439>
- Eshelby, J. D. (1957). The elastic model of lattice defects. *Annalen der Physik*, 456(1–3), 116–121. <https://doi.org/10.1002/andp.19574560113>
- Ferretti, A., Prati, C., & Rocca, F. (2001). Permanent scatterers in SAR interferometry. *IEEE Transactions on Geoscience and Remote Sensing*, 39(1), 8–20. <https://doi.org/10.1109/36.898661>
- Hanks, T. C., & Kanamori, H. (1979). A moment magnitude scale. *Journal of Geophysical Research*, 84(B5), 2348–2350. <https://doi.org/10.1029/JB084iB05p02348>
- Hansen, B. E. (1992). Testing for parameter instability in linear models. *Journal of Policy Modeling*, 14(4), 517–533. [https://doi.org/10.1016/0161-8938\(92\)90019-9](https://doi.org/10.1016/0161-8938(92)90019-9)
- Harris, R. A. (2017). Large earthquakes and creeping faults: Large earthquakes and creeping faults. *Reviews of Geophysics*, 55(1), 169–198. <https://doi.org/10.1002/2016RG000539>
- Hooper, A., Segall, P., & Zebker, H. (2007). Persistent scatterer interferometric synthetic aperture radar for crustal deformation analysis, with application to Volcán Alcedo, Galápagos. *Journal of Geophysical Research*, 112(B7), B07407. <https://doi.org/10.1029/2006JB004763>
- Hsu, Y.-J., Simons, M., Yu, S.-B., Kuo, L.-C., & Chen, H.-Y. (2003). A two-dimensional dislocation model for interseismic deformation of the Taiwan mountain belt. *Earth and Planetary Science Letters*, 211(3–4), 287–294. [https://doi.org/10.1016/s0012-821x\(03\)00203-6](https://doi.org/10.1016/s0012-821x(03)00203-6)
- Hsu, Y.-J., Yu, S.-B., & Chen, H.-Y. (2009). Coseismic and postseismic deformation associated with the 2003 Chengkung, Taiwan, earthquake. *Geophysical Journal International*, 176(2), 420–430. <https://doi.org/10.1111/j.1365-246X.2008.04009.x>
- Igarashi, T., Matsuzawa, T., & Hasegawa, A. (2003). Repeating earthquakes and interplate aseismic slip in the northeastern Japan subduction zone. *Journal of Geophysical Research*, 108(B5), 2249. <https://doi.org/10.1029/2002JB001920>
- Ikari, M. J., Marone, C., Saffer, D. M., & Kopf, A. J. (2013). Slip weakening as a mechanism for slow earthquakes. *Nature Geoscience*, 6(6), 468–472. <https://doi.org/10.1038/ngeo1818>
- Johnson, L. R., & Nadeau, R. M. (2002). Asperity model of an earthquake: Static problem. *Bulletin of the Seismological Society of America*, 92(2), 672–686. <https://doi.org/10.1785/0120000282>
- Kanamori, H., & Anderson, D. L. (1975). Theoretical basis of some empirical relations in seismology. *Bulletin of the Seismological Society of America*, 65(5), 1073–1095. <https://doi.org/10.1785/BSSA0650051073>
- Khoshmanesh, M., Shirzaei, M., & Nadeau, R. M. (2015). Time-dependent model of aseismic slip on the central San Andreas Fault from InSAR time series and repeating earthquakes. *Journal of Geophysical Research: Solid Earth*, 120(9), 6658–6679. <https://doi.org/10.1002/2015JB012039>
- Kubo, H., & Nishikawa, T. (2020). Relationship of preseismic, coseismic, and postseismic fault ruptures of two large interplate aftershocks of the 2011 Tohoku earthquake with slow-earthquake activity. *Scientific Reports*, 10(1), 1–10. <https://doi.org/10.1038/s41598-020-68692-x>
- Kuoehen, H., Wu, Y.-M., Chen, Y.-G., & Chen, R.-Y. (2007). 2003 Mw6.8 Chengkung earthquake and its related seismogenic structures. *Journal of Asian Earth Sciences*, 31(3), 332–339. <https://doi.org/10.1016/j.jseas.2006.07.028>
- Lee, J.-C., Chu, H.-T., Angelier, J., Hu, J.-C., Chen, H.-Y., & Yu, S.-B. (2006). Quantitative analysis of surface coseismic faulting and postseismic creep accompanying the 2003, Mw = 6.5, Chengkung earthquake in eastern Taiwan. *Journal of Geophysical Research*, 111(B2), B02405. <https://doi.org/10.1029/2005JB003612>
- Lee, S.-J., Liu, T.-Y., & Lin, T.-C. (2023). The role of the west-dipping collision boundary fault in the Taiwan 2022 Chihshang earthquake sequence. *Scientific Reports*, 13(1), 3552. <https://doi.org/10.1038/s41598-023-30361-0>
- Liu, C.-C., & Yu, S.-B. (1990). Vertical crustal movements in eastern Taiwan and their tectonic implications. *Tectonophysics*, 183(1), 111–119. [https://doi.org/10.1016/0040-1951\(90\)90191-A](https://doi.org/10.1016/0040-1951(90)90191-A)
- Mavrommatis, A. P., Segall, P., Uchida, N., & Johnson, K. M. (2015). Long-term acceleration of aseismic slip preceding the Mw 9 Tohoku-oki earthquake: Constraints from repeating earthquakes. *Geophysical Research Letters*, 42(22), 9717–9725. <https://doi.org/10.1002/2015GL066069>
- Mozziconacci, L., Delouis, B., Huang, B., Lee, J., & Béthoux, N. (2013). Determining fault geometry from the distribution of coseismic fault slip related to the 2006 Taitung Earthquake, Eastern Taiwan. *Bulletin of the Seismological Society of America*, 103(1), 394–411. <https://doi.org/10.1785/0120110232>
- Nadeau, R. M., Foxall, W., & McEvilly, T. (1995). Clustering and periodic recurrence of microearthquakes on the San Andreas Fault at Parkfield, California. *Science (New York, N.Y.)*, 267(5197), 503–507. <https://doi.org/10.1126/science.267.5197.503>
- Nadeau, R. M., & Johnson, L. R. (1998). Seismological studies at Parkfield VI: Moment release rates and estimates of source parameters for small repeating earthquakes. *Bulletin of the Seismological Society of America*, 88(3), 790–814. <https://doi.org/10.1785/BSSA0880030790>
- Nadeau, R. M., & McEvilly, T. V. (1999). Fault slip rates at depth from recurrence intervals of repeating microearthquakes. *Science*, 285(5428), 718–721. <https://doi.org/10.1126/science.285.5428.718>
- Nadeau, R. M., & McEvilly, T. V. (2004). Periodic pulsing of characteristic microearthquakes on the San Andreas Fault. *Science*, 303(5655), 220–222. <https://doi.org/10.1126/science.1090353>

- Okada, Y. (1992). Internal deformation due to shear and tensile faults in a half-space. *Bulletin of the Seismological Society of America*, 82(2), 1018–1040. <https://doi.org/10.1785/BSSA0820021018>
- Peng, W. (2023). Weipengtw/Chihshang_inversion: Chihshang_inversion_file [Dataset]. Zenodo. <https://doi.org/10.5281/zenodo.8226653>
- Peng, W., Marsan, D., Chen, K., & Pathier, E. (2021). Earthquake swarms in Taiwan: A composite declustering method for detection and their spatial characteristics. *Earth and Planetary Science Letters*, 574, 117160. <https://doi.org/10.1016/j.epsl.2021.117160>
- Radiguet, M., Cotton, F., Vergnolle, M., Campillo, M., Valette, B., Kostoglodov, V., & Cotte, N. (2011). Spatial and temporal evolution of a long term slow slip event: The 2006 Guerrero Slow Slip Event. *Geophysical Journal International*, 184(2), 816–828. <https://doi.org/10.1111/j.1365-246X.2010.04866.x>
- Sammis, C. G. (2001). Repeating earthquakes as low-stress-drop events at a border between locked and creeping fault patches. *Bulletin of the Seismological Society of America*, 91(3), 532–537. <https://doi.org/10.1785/0120000075>
- Savage, J. C. (1983). A dislocation model of strain accumulation and release at a subduction zone. *Journal of Geophysical Research*, 88(B6), 4984–4996. <https://doi.org/10.1029/JB088iB06p04984>
- Scholz, C. H. (1998). Earthquakes and friction laws. *Nature*, 391(6662), 37–42. <https://doi.org/10.1038/34097>
- Shyu, J. B. H., Chung, L.-H., Chen, Y.-G., Lee, J.-C., & Sieh, K. (2007). Re-evaluation of the surface ruptures of the November 1951 earthquake series in eastern Taiwan, and its neotectonic implications. *Journal of Asian Earth Sciences*, 31(3), 317–331. <https://doi.org/10.1016/j.jseas.2006.07.018>
- Shyu, J. B. H., Sieh, K., Chen, Y.-G., Chung, L.-H., & Chung, L. H. (2006). Geomorphic analysis of the Central Range fault, the second major active structure of the Longitudinal Valley suture, eastern Taiwan. *GSA Bulletin*, 118(11–12), 1447–1462. <https://doi.org/10.1130/B25905.1>
- Shyu, J. B. H., Sieh, K., Chen, Y.-G., & Liu, C.-S. (2005). Neotectonic architecture of Taiwan and its implications for future large earthquakes. *Journal of Geophysical Research*, 110(B8), B08402. <https://doi.org/10.1029/2004JB003251>
- Shyu, J. B. H., Wang, Y., & Zhou, H. N. (2023). The Central Range Fault System: Knowledge from the surface rupture characteristics of the September 2022 Guanshan-Chihshang Earthquake Series. *Sino-Geotechnics*, 1(176), 7–14.
- Tarantola, A. (2005). *Inverse problem theory and methods for model parameter estimation*. Society for Industrial and Applied Mathematics. <https://doi.org/10.1137/1.9780898717921>
- The MathWorks Inc. (2022). MATLAB version: 9.13.0 (R2022b) [Software]. The MathWorks Inc. Retrieved from <https://www.mathworks.com>
- Thomas, M. Y., Avouac, J.-P., Champenois, J., Lee, J.-C., & Kuo, L.-C. (2014). Spatiotemporal evolution of seismic and aseismic slip on the Longitudinal Valley fault, Taiwan. *Journal of Geophysical Research: Solid Earth*, 119(6), 5114–5139. <https://doi.org/10.1002/2013JB010603>
- Tsai, M.-C., Yu, S.-B., Shin, T.-C., Kuo, K.-W., Leu, P.-L., Chang, C., & Ho, M.-Y. (2015). Velocity field derived from Taiwan continuous GPS Array (2007–2013). *Terrestrial, Atmospheric and Oceanic Sciences*, 26(5), 527. [https://doi.org/10.3319/TAO.2015.05.21.01\(T\)](https://doi.org/10.3319/TAO.2015.05.21.01(T))
- Uchida, N., & Bürgmann, R. (2019). Repeating earthquakes. *Annual Review of Earth and Planetary Sciences*, 47(1), 305–332. <https://doi.org/10.1146/annurev-earth-053018-060119>
- Uchida, N., Matsuzawa, T., Hasegawa, A., & Igarashi, T. (2003). Interplate quasi-static slip off Sanriku, NE Japan, estimated from repeating earthquakes: Interplate slip off Sanriku, from repeating earthquakes. *Geophysical Research Letters*, 30(15), 1801. <https://doi.org/10.1029/2003GL017452>
- Wang, K., & Bilek, S. L. (2014). Invited review paper: Fault creep caused by subduction of rough seafloor relief. *Tectonophysics*, 610, 1–24. <https://doi.org/10.1016/j.tecto.2013.11.024>
- Wessel, P., Smith, W. H. F., Scharroo, R., Luis, J., & Wobbe, F. (2013). Generic Mapping Tools: Improved version released [Software]. *Eos, Transactions, American Geophysical Union*, 94(45), 409–410. <https://doi.org/10.1002/2013EO450001>
- Wesson, R. L., & Nicholson, C. (1988). Intermediate-term, pre-earthquake phenomena in California, 1975–1986, and preliminary forecast of seismicity for the next decade. *Pure and Applied Geophysics*, 126(2), 407–446. <https://doi.org/10.1007/BF00879005>
- Wu, Y.-M., Chen, Y.-G., Chang, C.-H., Chung, L.-H., Teng, T.-L., Wu, F. T., & Wu, C.-F. (2006). Seismogenic structure in a tectonic suture zone: With new constraints from 2006 Mw6.1 Taitung earthquake. *Geophysical Research Letters*, 33(22), L22305. <https://doi.org/10.1029/2006GL027572>

References From the Supporting Information

- Tang, C.-H., Lin, Y. N., Tung, H., Wang, Y., Lee, S.-J., Hsu, Y.-J., et al. (2023). Interactions between the dual-verging thrust faults in eastern Taiwan revealed by the 2022 Chihshang earthquake sequence and centennial historical seismicity. In *EGU General Assembly 2023, Vienna, Austria*, 24–28 Apr 2023, EGU23-4292. <https://doi.org/10.5194/egusphere-egu23-4292>